The Astronomical Journal, 141:57 (24pp), 2011 February doi:10.1088/0004-6256/141/2/57


# PHYSICAL PROPERTIES OF COMPLEX C HALO CLOUDS

W.-H. Hsu[1], M. E. Putman[2], F. Heitsch[3], S. Stanimirović[4], J. E. G. Peek[2], and S. E. Clark[3]
[1] Department of Astronomy, University of Michigan, Ann Arbor, MI 48109, USA; wenhsin@umich.edu
[2] Department of Astronomy, Columbia University, New York, NY 10027, USA
[3] Department of Physics & Astronomy, University of North Carolina at Chapel Hill, Chapel Hill, NC 27599, USA
[4] Department of Astronomy, University of Wisconsin-Madison, Madison, WI 53706-1582, USA
*Received 2010 February 1; accepted 2010 November 7; published 2011 January 13*

## ABSTRACT

Observations from the Galactic Arecibo L-band Feed Array H I (GALFA-H I) Survey of the tail of Complex C are presented and the halo clouds associated with this complex are cataloged. The properties of the Complex C clouds are compared to clouds cataloged at the tail of the Magellanic Stream to provide insight into the origin and destruction mechanism of Complex C. Magellanic Stream and Complex C clouds show similarities in their mass distributions (slope $= -0.7$ and $-0.6$ $\log(N(\log(\mathrm{mass})))/\log(\mathrm{mass})$, respectively) and have a common line width of 20–30 km s$^{-1}$ (indicative of a warm component), which may indicate a common origin and/or physical process breaking down the clouds. The clouds cataloged at the tail of Complex C extend over a mass range of $10^{1.1}$–$10^{4.8}$ $M_\odot$, sizes of $10^{1.2}$–$10^{2.6}$ pc, and have a median volume density and pressure of 0.065 cm$^{-3}$ and $(P/k) =$ 580 K cm$^{-3}$. We do not see a prominent two-phase structure in Complex C, possibly due to its low metallicity and inefficient cooling compared to other halo clouds. Assuming that the Complex C clouds are in pressure equilibrium with a hot halo medium, we find a median halo density of $5.8 \times 10^{-4}$ cm$^{-3}$, which given a constant distance of 10 kpc is at a $z$-height of $\sim$3 kpc. Using the same argument for the Stream results in a median halo density of $8.4 \times 10^{-5}$(60 kpc/d) cm$^{-3}$. These densities are consistent with previous observational constraints and cosmological simulations. We also assess the derived cloud and halo properties with three-dimensional grid simulations of halo H I clouds and find that the temperature is generally consistent within a factor of 1.5 and the volume densities, pressures, and halo densities are consistent within a factor of three.

*Key words:* Galaxy: formation – Galaxy: halo – intergalactic medium – ISM: clouds – ISM: structure

*Online-only material:* color figures

## 1. INTRODUCTION

The origin and role of the neutral hydrogen (H I) gas clouds located in the Galactic Halo is subject to much debate. The suggested origin models include condensed gas originating from the "Galactic fountain" (Shapiro & Field 1976; Bregman 1980; Fraternali & Binney 2008), warm/hot halo gas cooling and fragmenting during the cooling process (e.g., Maller & Bullock 2004; Kaufmann et al. 2006; Sommer-Larsen 2006; Kereš & Hernquist 2009) and gas stripped from the dwarf galaxies (e.g., Putman et al. 2003), with a combination of the models being most likely. These halo clouds, aka high-velocity clouds (HVCs), potentially play a key role in galaxy evolution. Chemical evolution models of the Galaxy suggest that an infall of low-metallicity gas at the rate of $\sim$1 $M_\odot$ per year is needed to explain the metallicity of the G and K stars in the solar neighborhood (Chiappini et al. 2001; Fenner & Gibson 2003; Robitaille & Whitney 2010) and our Galaxy is forming stars at a rate that seems to require continual re-fueling. Galaxy formation simulations also suggest a galaxy gradually acquires its star formation fuel over time, and HVCs trace this ongoing process (e.g., Peek et al. 2008; Kereš & Hernquist 2009).

Complex C and the Magellanic Stream are the largest and most massive HVCs in the Galactic sky (approximately $M_{\mathrm{H\,I}} = 5 \times 10^6$ and $2 \times 10^8$ $M_\odot$, respectively; Thom et al. 2008; Putman et al. 2003). While the Magellanic Stream has a known origin as being ripped from our dwarf companions, the Magellanic Clouds, Complex C's origin has remained a mystery. The argument that Complex C is a low-metallicity infalling extragalactic cloud (Wakker et al. 1999) has been challenged by several subsequent authors, who find a metallicity range between 0.1 and 0.5 solar across the cloud (Gibson et al. 2001; Collins et al. 2003, 2007; Tripp et al. 2003). This may indicate that Complex C is actually a mixture of infalling gas and "Galactic fountain" gas, or possibly the stripped baryonic component of a dark matter halo.

Complex C is elongated and extends from 140° to 30° in Galactic longitude and 65° to 10° in Galactic latitude. The tail of Complex C is therefore approaching the Galactic plane and may trace the accretion of halo gas onto the disk. Recent distance constraints have opened up new possibilities for studies of the physical properties of Complex C (e.g., mass, physical size). Thom et al. (2008) used halo stars to set upper and lower distance constraints on the complex and place it at $10 \pm 2.5$ kpc (see also Wakker et al. 2007). They use this information to derive the total mass of the complex and estimate an accretion rate of 0.1 $M_\odot$ yr$^{-1}$ from this HVC alone.

Both Complex C and the Magellanic Stream are thought to be embedded in a hot diffuse halo medium, as this halo medium is both detected indirectly observationally and expected from galaxy formation simulations. The observational evidence for this halo medium includes: O VI absorption lines associated with the HVCs which are thought to originate from collisional ionization as the clouds interact with the ambient medium (Sembach et al. 2003); head–tail structures of the HVCs, or a compressed head and diffuse tail (e.g., Heitsch & Putman 2009; Brüns et al. 2000); shearing structures on the H I complexes (Peek et al. 2007); confinement of the Magellanic Stream (Stanimirović et al. 2002); and the two-phase velocity structure of the clouds, implying that the HVCs lie in a medium of significant pressure (Wolfire et al. 1995b, hereafter W95; Kalberla & Haud 2006). Recent simulations indicate the hot

halo medium fills the dark matter halo (∼150 kpc) and hosts a large fraction of a galaxy's baryons (Maller & Bullock 2004; Sommer-Larsen 2006; Kaufmann et al. 2008). This halo medium most likely originates from a combination of the initial baryon collapse and Galaxy feedback mechanisms, but its properties at a range of radii remain to be determined as it is extremely difficult to detect directly due to its hot, diffuse nature. Detailed H I observations of halo clouds at a range of distances can be used to probe this elusive, diffuse halo medium.

In this paper, we present new H I observations of the tail of Complex C from the Galactic Arecibo L-band Feed Array H I (GALFA-H I) Survey (Section 2), catalog the clouds for this region and for the tail of the Magellanic Stream (Section 3), and derive the physical properties of the clouds (Section 4). We test the derivation of some of these physical properties with simulations in Section 5. Previous H I observations of large sections of Complex C have been limited to observations with a 36′ beam (Wakker et al. 1999; Kalberla & Haud 2006), while the GALFA-H I observations provide 3.′5 spatial resolution and up to 0.18 km s$^{-1}$ velocity resolution (smoothed to 1.4 km s$^{-1}$ for this work). The GALFA-H I observations of the Magellanic Stream were previously published (Stanimirović et al. 2008, hereafter S08) and are cataloged and analyzed further here. In Section 6, we compare the Complex C and Magellanic Stream cloud populations, investigate the physical underpinnings of the lack of two-phase structure in the clouds, and calculate the density of their surrounding diffuse hot halo through pressure-balance arguments. The results provide insight into the physical properties of halo gas and the nature of HVCs as they disrupt within the halo.

## 2. OBSERVATIONS AND DATA REDUCTION

### 2.1. Observations

The H I data presented here were obtained with the GALFA-H I spectrometer (galspect) on the Arecibo Radio Telescope (Stanimirović et al. 2006). GALFA-H I data provide a channel spacing of 0.18 km s$^{-1}$ and cover a maximum velocity range of −765 to +765 km s$^{-1}$ (LSR). The spatial resolution is approximately 3.′5. The data presented here will be included in the GALFA-H I Survey of the entire Arecibo sky and are publicly available at https://purcell.ssl.berkeley.edu.

The Complex C data were taken as part of a proposal to map high and intermediate velocity clouds at the disk–halo interface (A2060). The observations were taken in "basketweave mode." The telescope is pointed at the meridian but moves up and down in zenith angle. Each day the starting point was offset in R.A. so that the entire region of interest was covered. The advantage of this observing mode is that it generates a large number of crossing points which can be used in the crossing-point calibration (see Section 2.2).

The Complex C map covers a region of $17^h20^m$ to $18^h10^m$ in R.A. and 2° to 14° in decl., corresponding to approximately $(l, b) = (25°–40°, 12°–24°,)$ in Galactic coordinates. We did two passes of this region to increase sensitivity and minimize the effects of interference. The cube used to catalog clouds associated with the tail of the Magellanic Stream has been presented in S08. The Stream data cube is made up of both "basketweave" and drift scans. In this paper, we consider only the regions with the lowest noise level. The first region (referred to as region 1) extends from $22^h0^m$ to $23^h30^m$ in R.A. and 15.°5 to 23° in decl., corresponding to $(l, b) = (77°–97°, -41°$to $-28°)$ and the second region (referred to as region 2) extends from $22^h0^m$ to $23^h50^m$ in R.A. and 11.°75 to 16° in decl., corresponding to $(l, b) = (72°$ to $100°, -48°$to $-32°)$.

### 2.2. Data Reduction

The data reduction includes the following steps, the details of which are outlined in Peek & Heiles (2008, hereafter PH08).

1. *Calibration using least-squares frequency switching*. The least-squares frequency switching (Heiles 2007) is used for GALFA-H I observations because it is impossible to find an "off-target" region without Galactic emission near 0 km s$^{-1}$ that can be used in calibration. At the beginning of each observation, data from a single position are taken at several frequencies. This technique is able to separate the intermediate frequency (IF) gain spectrum from the radio frequency (RF) power spectrum, and thus the IF gain spectrum can be applied to all the spectra taken in that day.
2. *Ripple removal*. Ripples due to known sources (reflection in the signal chain) are removed from the spectra. Since the geometry of the reflection is known, the Fourier components corresponding to these ripples can be easily removed. To remove the ripple caused by the reflection in the telescope superstructure and geodetic dome is more difficult. The average of all seven beams is taken and subtracted from the average of one beam in a day. Then the resulting spectrum is searched for baseline ripples over the periods of 0.5–2 $\mu$s.
3. *Crossing-point calibration*. At each crossing point, the sky is observed multiple times, and the dominating source of the difference in the spectra should be the variation in gain. The crossing points can be used in determining the relative gains of each beam over each day. The relative gain information is then applied to the calibration process and greatly reduces the effect of gain variation on the data.
4. *Gridding*. The time-ordered spectra are gridded into the data cubes. The GALFA-H I Survey cubes are gridded into two formats, depending on the velocity region of interest and kinematic resolution required. We chose to work with the cubes that have the entire GALFA-H I velocity range and have the channels smoothed to 0.74 km s$^{-1}$. The cubes all have a 1′ pixel size.

The data used here have not been corrected for first sidelobes. Sidelobe calibration can be implemented in the future to improve the data quality (Putman et al. 2009), and may increase the peak brightness temperatures of the clouds by at most 10%, and decrease the cloud sizes by a similar amount. See Section 6.6 in PH08 for details.

The rms noise level of the Complex C cube is about 0.06 K for channels smoothed to 1.4 km s$^{-1}$. The 3$\sigma$ sensitivity is $4.5 \times 10^{17}$ cm$^{-2}$ per 1.4 km s$^{-1}$ The 5$\sigma$ mass sensitivity to a cloud at 10 kpc with 25 km s$^{-1}$ line width is ∼18 $M_\odot$. The rms noise level of the Stream cube is 0.05 K for region 1 and 0.03 K for region 2 for channels smoothed to 1.4 km s$^{-1}$. The 3$\sigma$ sensitivity of the Stream cube is $4.3 \times 10^{17}$cm$^{-2}$ per 1.4 km s$^{-1}$ for region 1 and $2.3 \times 10^{17}$ cm$^{-2}$ for region 2. See S08 for further details.

Figures 1 and 2 show the integrated intensity and average velocity maps of Complex C in Galactic coordinates, respectively. These figures have been created after removing Galactic emission (described in Section 3.1) and isolating the gas associated with Complex C ($V_{LSR}$ −190 to −65 km s$^{-1}$ as evident in the channel maps and cloud catalogs).

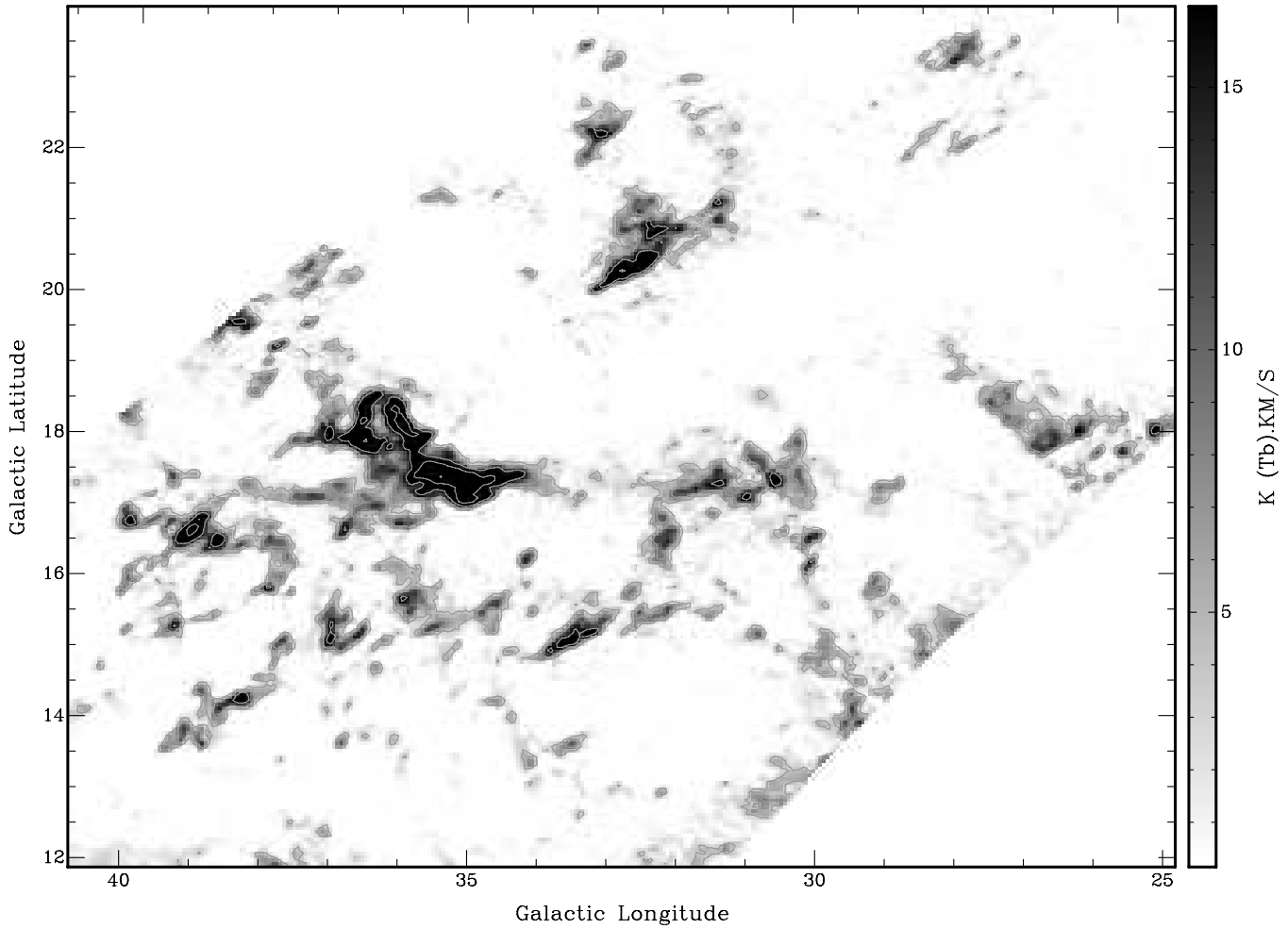


**Figure 1.** Integrated intensity map for the tail of Complex C in Galactic coordinates. The map covers $V_{LSR} = -190$ to $-65$ km s$^{-1}$. Contours are 4, 8, 16, 32, and 64 K km s$^{-1}$, corresponding to column densities of $7.3 \times 10^{18}$, $1.5 \times 10^{19}$, $2.9 \times 10^{19}$, $5.8 \times 10^{19}$, and $1.2 \times 10^{20}$ cm$^{-2}$.

## 3. CLOUD CATALOGS

To quantify the properties of individual clouds within the complexes we used an automated cloud finder called Duchamp (Whiting 2008). This program searches for groups of connected voxels that are above a certain $T_b$ threshold and avoids bias introduced by cataloguing the clouds by eye. Automating the cloud finding also allows us to quantify the depth of the search and how clouds are merged together. This is particularly important for the results of this paper, giving us unbiased statistics of the cloud properties and allowing for a comparison of the clouds from two complexes.

### *3.1. Cloud Search—Duchamp Source Finder*

We applied Duchamp to the GALFA-H I cubes of the Magellanic Stream and Complex C as outlined below. We also used Duchamp on a heavily spatially smoothed version of the Complex C cube to approximate observing the complex at a larger distance. The steps used in the cloud cataloguing are summarized below, and the cataloguing parameters are summarized in Table 1.

1. The cubes are smoothed spatially to 3′ by 3′ per pixel and spectrally to 1.42 km s$^{-1}$. This increases the efficiency of the cloud finder by improving the signal-to-noise ratio and having fewer pixels to search.

**Table 1**
Cloud Cataloging Parameters

| HVC Complex | $\Delta x$ [a] (′) | $\Delta v$ [b] (km s$^{-1}$) | Detection $\sigma$ [c] (K) | Grow $\sigma$ [d] (K) | $V_{LSR}$ Range (km s$^{-1}$) |
|---|---|---|---|---|---|
| Complex C | 3 | 1.42 | 0.29 | 0.18 | −200 to − 50 |
| Complex C (smoothed) | 18 | 1.42 | 0.12 | 0.08 | −200 to − 50 |
| MS (region 1) | 3 | 1.42 | 0.27 | 0.17 | −420 to − 280 |
| MS (region 2) | 3 | 1.42 | 0.15 | 0.09 | −420 to − 280 |

**Notes.**
[a] Angular resolution of the searched cube.
[b] Velocity resolution of the searched cube.
[c] Primary detection threshold.
[d] Grow threshold: pixels above the grow threshold neighboring a detected pixel will be added to the detection.

2. The robust statistics, the median and the median absolute deviation from the median (MADFM), are calculated from all the pixels and channels in the entire search region. The detection threshold for the cloud search is set at a fixed value n times the MADFM above the median ($n\sigma$) specified by the user.

3. The data cube is searched for all pixels above the detection threshold. Once a pixel is found above the detection threshold, the size of the detection is increased by adding

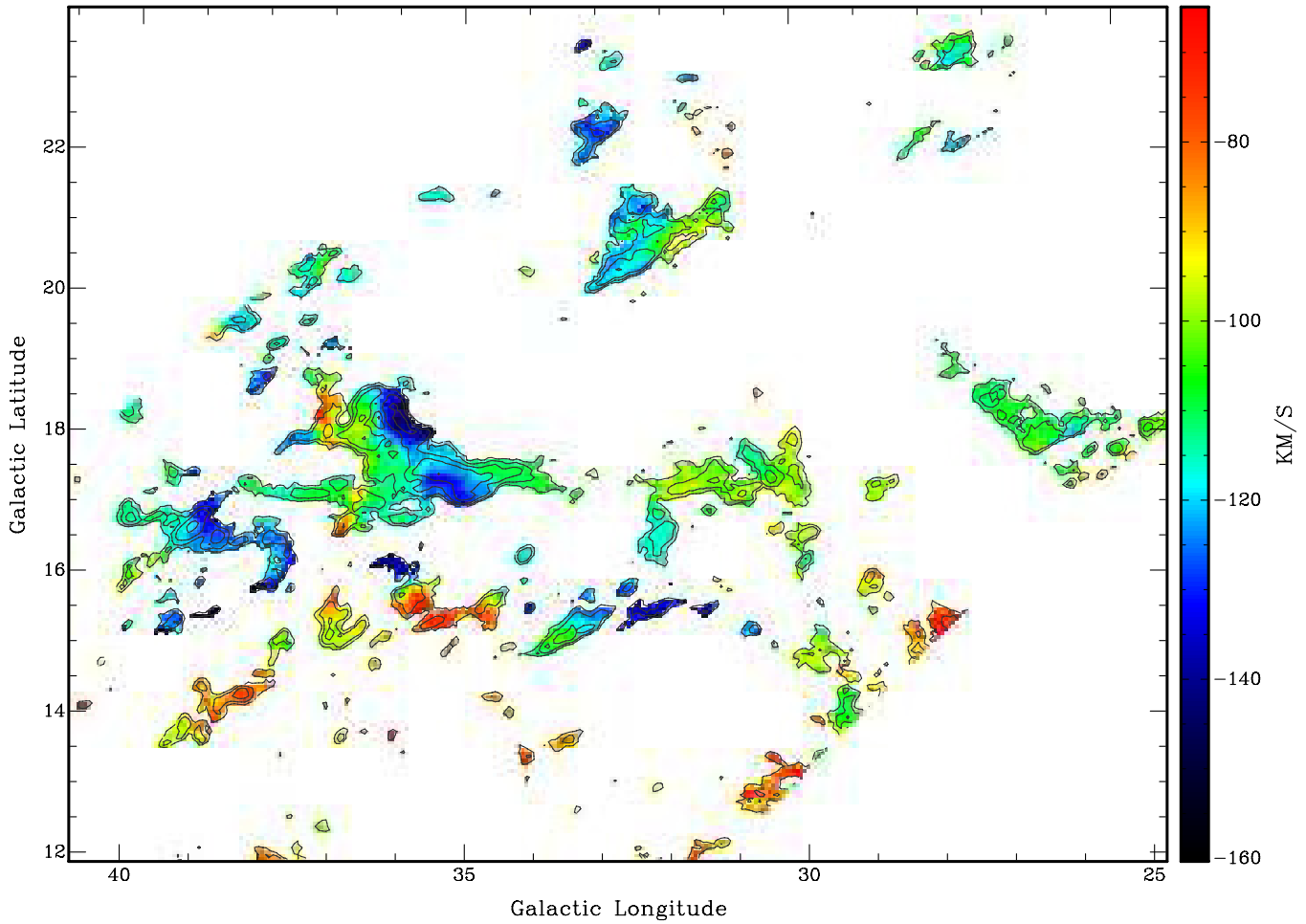


**Figure 2.** LSR velocity map of Complex C with the integrated intensity contours from Figure 1 overlaid. The map covers $V_{\rm LSR} = -190$ to $-65$ km s$^{-1}$. A small fraction of clouds have $V_{\rm LSR} < -160$ km s$^{-1}$ and are colored black in this map.

(A color version of this figure is available in the online journal.)

nearby pixels that are above a secondary threshold, or the "grow parameter," specified by the user.

4. If two detections are adjacent to each other after step 3, the detections are merged into one.
5. All the detections from step 4 are automatically screened by Duchamp for false detections. To minimize this number, we specify that the detections must span a minimum of four channels (5.6 km s$^{-1}$) and two pixels ($\approx 6'$) to be included in the output list.
6. All the detections in the output list are then examined by eye. Detections that are possibly due to scanning artifacts or radio frequency interface (RFI) are excluded from the final list.

The output of Duchamp provides the following information: R.A. and decl. of the cloud, size of the cloud in R.A. and decl., and the total spectrum of all the detected pixels. A Gaussian fitting program was subsequently used to fit up to two Gaussian profiles to the spectrum of each cloud. We only adopt the result of the two-Gaussian fit if it improves the rms error by more than 5%. The line width, central velocity, and total H I column density of the cloud were determined from this Gaussian fitting. The parameters used to search the Complex C and Magellanic Stream cubes and the cataloguing results are summarized in the next two sections.

There was an additional step to the above list in the case of Complex C. Since Complex C extends into less negative velocities where Galactic emission becomes important, the noise level in the Complex C data is not constant throughout the spectrum. It is difficult to use Duchamp directly on the cube in this case because Duchamp only uses the global statistics of the cube. To solve this problem, we made an effort to remove Galactic emission from the cube. Since diffuse Galactic emission does not change dramatically over the spatial region of the Complex C cube, we determine the contamination of Galactic emission by using a few small patches where there are no discrete H I clouds. The size of each patch is $30' \times 30'$, and the patches are roughly 3–4 deg apart. The distance weighted average spectrum of these patches is then subtracted from the $-250$ to $-40$ km s$^{-1}$ range of each spectrum in the cube. This step is done after the cube is smoothed into $3' \times 3'$ pixels and before cloud searching (i.e., between steps 1 and 2). This made it possible to catalog discrete clouds at low velocity and also gives a more accurate mass for these clouds. Figure 3 shows examples of cloud spectra before and after removing Galactic emission.

### 3.2. Complex C Cloud Catalog

We ran Duchamp twice on the Complex C cube; once at the full resolution ($3'.5$) and once smoothed to a resolution equivalent of moving Complex C to a distance more appropriate for the Magellanic Stream (60 kpc, $18'$). We used a detection threshold of 0.29 K ($5\sigma$) on the original cube and 0.12 K ($5\sigma$)

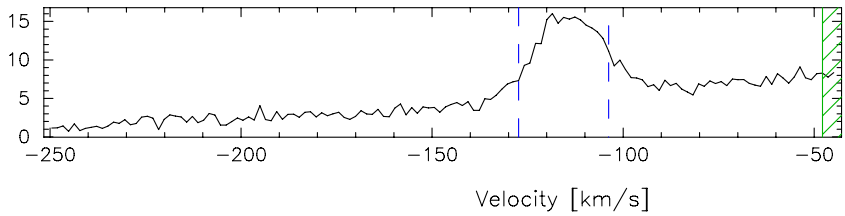


(a) Spectrum of cloud 35 before removing Galactic emission

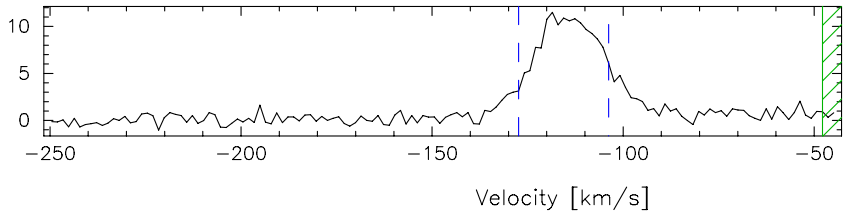


(b) Spectrum of cloud 35 after removing Galactic emission

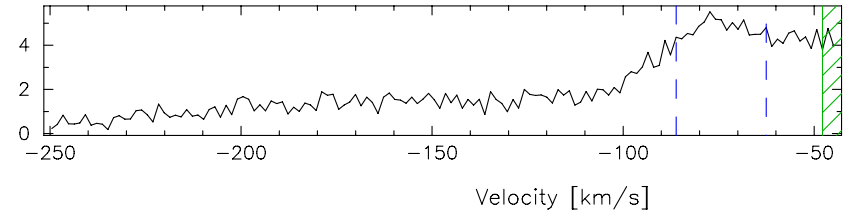


(c) Spectrum of cloud 77 before removing Galactic emission

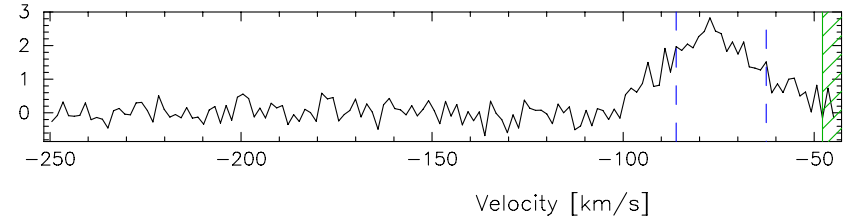


(d) Spectrum of cloud 77 after removing Galactic emission

**Figure 3.** Two examples of the integrated spectra of cataloged Complex C clouds before and after removing Galactic emission (labeled 35 and 77 in Figure 4). In the case of cloud 35, the cloud would be easily identified by Duchamp without Galactic removal (but with an elevated flux). In the case of cloud 77, removing Galactic emission makes it much easier to identify the cloud. The units on the *y*-axis of the spectra represent the sum of the brightness temperatures of all pixels associated with cloud and the hatching to right represents the velocity region not considered in the cataloging due to stronger Galactic emission.

(A color version of this figure is available in the online journal.)

on the smoothed cube, and grew the detected clouds to $3\sigma$ (0.18 K on the original cube, and 0.08 K on the smoothed cube). The search parameters are tabulated in Table 1. The velocity range searched for clouds was $-200$ to $-50$ km s$^{-1}$. Figure 4 shows the integrated intensity maps of the Duchamp detections for the original Complex C cube and the smoothed cube. We inspected each of the Duchamp detections by eye after running the program (step 6). About 15% of the Duchamp detections (20 out of 134) were removed due to their identification as remnant scanning artifacts (detections which generally only extend over a few pixels and/or channels or obviously follow the basket weave pattern) and an additional 21 clouds were removed because a large percentage of their emission was located at the edge of our search area (i.e., velocity center lies near or above $-50$ km s$^{-1}$). An example spectrum of a real Duchamp detection in Complex C is shown in Figure 3. Only the real clouds with $V_{\rm LSR} < -65$ km s$^{-1}$ are cataloged in Table 2. Clouds between $V_{\rm LSR} = -65$ and $-50$ km s$^{-1}$ are cataloged in Table 3.

The cloud catalogs contain the following entries.

*Column 1*. Cloud number. Here we use the cloud numbers assigned by Duchamp (shown in Figure 4; Figure 7 for the Magellanic Stream). The missing numbers are clouds removed after examining each Duchamp detection by eye.

*Columns 2 and 3*. R.A. and decl. (J2000) as provided by Duchamp. These are the intensity-weighted average centroid positions.

*Columns 4 and 5*. Galactic longitude and latitude obtained from the R.A. and decl. in Columns 2 and 3.

*Columns 6 and 7*. Angular size in R.A. and decl. The angular size is given by Duchamp and is the total size of the cloud down to $3\sigma$ level. At the distance of 10 kpc, the conversion between angular size and physical size is given by $1' = 2.9$ pc.

*Column 8*. Peak brightness temperature in K.

*Column 9*. Local Standard of Rest (LSR) velocity. Centroid determined by Gaussian fitting of the total cloud spectrum.

*Column 10*. Velocity in the Galactic Standard of Rest (GSR) frame, defined as $V_{\rm GSR} = 220 \cdot \cos(b)\sin(l) + V_{\rm LSR}$.

*Column 11*. Width of the Gaussian used to fit the spectrum in km s$^{-1}$, defined as the FWHM of the Gaussian.

*Column 12*. Total H I column density of the cloud, in units of $10^{18}$ cm$^{-2}$.

**Table 2**
Complex C Cloud Catalog

| Cloud | R.A. (J2000) | Decl. (J2000) | $l$ (°) | $b$ (°) | ΔR.A.[a] (′) | ΔDecl.[a] (′) | $T_{b,\mathrm{peak}}$ (K) | $V_{\mathrm{LSR}}$ (km s$^{-1}$) | $V_{\mathrm{GSR}}$ (km s$^{-1}$) | $\Delta V$ (km s$^{-1}$) | $N_{\mathrm{H\,I}}$(tot) ($10^{18}$ cm$^{-2}$) | $M_{\mathrm{H\,I}}$[b] ($M_{\odot}$) |
|---|---|---|---|---|---|---|---|---|---|---|---|---|
| 1 | 18:05:41 | +11:05:57 | 37.84 | 15.13 | 20.6 | 18.0 | 0.33 | −177.9 | −47.6 | 20.8 | 126.8 | 77.4 |
| 2 | 18:06:28 | +11:25:00 | 38.22 | 15.09 | 8.8 | 6.0 | 0.29 | −175.2 | −43.7 | 22.0 | 20.6 | 12.6 |
| 3 | 18:06:25 | +11:38:03 | 38.42 | 15.19 | 8.8 | 12.0 | 0.38 | −172.5 | −40.6 | 21.8 | 64.8 | 39.5 |
| 4 | 18:03:51 | +10:47:21 | 37.35 | 15.40 | 29.5 | 33.0 | 0.37 | −166.0 | −37.3 | 25.2 | 324.5 | 197.9 |
| 5 | 18:01:30 | +10:26:26 | 36.77 | 15.77 | 29.5 | 24.0 | 0.56 | −162.6 | −35.9 | 25.1 | 354.5 | 216.3 |
| 6 | 17:52:23 | +05:11:35 | 30.84 | 15.49 | 65.7 | 99.0 | 0.57 | −134.0 | −25.3 | 30.8 | 2568.4 | 1566.7 |
| 7 | 17:57:37 | +08:50:35 | 34.84 | 15.94 | 47.4 | 66.0 | 0.75 | −133.0 | −12.1 | 28.1 | 1210.0 | 738.1 |
| 9 | 17:55:32 | +06:44:08 | 32.64 | 15.48 | 23.8 | 21.0 | 0.39 | −129.1 | −14.8 | 28.8 | 257.2 | 156.9 |
| 10 | 17:53:52 | +13:20:06 | 38.69 | 18.69 | 35.0 | 33.0 | 0.59 | −130.6 | −0.3 | 24.6 | 648.4 | 395.5 |
| 11 | 17:34:07 | +12:08:17 | 35.39 | 22.57 | 11.7 | 12.0 | 0.38 | −131.0 | −13.3 | 19.3 | 92.0 | 56.1 |
| 12 | 17:34:24 | +14:24:58 | 37.68 | 23.44 | 20.3 | 21.0 | 0.65 | −130.0 | −6.6 | 21.0 | 253.4 | 154.6 |
| 13 | 17:50:40 | +03:38:16 | 29.20 | 15.17 | 15.0 | 24.0 | 0.48 | −129.4 | −25.8 | 29.9 | 317.3 | 193.6 |
| 14 | 17:51:08 | +05:14:55 | 30.75 | 15.80 | 12.0 | 12.0 | 0.32 | −126.6 | −18.4 | 30.0 | 63.0 | 38.5 |
| 15 | 17:37:02 | +12:50:36 | 36.40 | 22.22 | 52.7 | 81.0 | 0.76 | −127.0 | −6.1 | 26.0 | 2855.4 | 1741.8 |
| 16 | 17:33:05 | +12:32:49 | 35.68 | 22.97 | 26.4 | 33.0 | 0.42 | −124.7 | −6.5 | 22.7 | 346.1 | 211.1 |
| 17 | 17:55:53 | +07:16:23 | 33.18 | 15.64 | 23.8 | 27.0 | 0.45 | −123.9 | −8.0 | 22.2 | 304.1 | 185.5 |
| 18 | 17:47:49 | +03:15:59 | 28.52 | 15.63 | 21.0 | 39.0 | 0.35 | −123.0 | −21.8 | 22.1 | 263.2 | 160.6 |
| 19 | 18:02:42 | +11:19:28 | 37.73 | 15.88 | 26.5 | 24.0 | 0.41 | −121.1 | 8.4 | 24.0 | 346.1 | 211.1 |
| 20 | 17:51:36 | +12:45:53 | 37.90 | 18.95 | 43.9 | 63.0 | 0.41 | −120.7 | 7.1 | 23.6 | 1217.2 | 742.5 |
| 21 | 17:28:21 | +08:01:20 | 30.71 | 22.10 | 53.5 | 36.0 | 0.45 | −119.6 | −15.5 | 24.6 | 637.0 | 388.6 |
| 22 | 17:53:45 | +07:30:06 | 33.15 | 16.22 | 23.8 | 21.0 | 1.38 | −119.6 | −4.1 | 5.9 | 85.1 | 51.9 |
| | | | | | | | | −118.3 | −2.7 | 20.7 | 383.5 | 233.9 |
| 23 | 17:39:37 | +10:29:11 | 34.39 | 20.66 | 109.2 | 147.0 | 1.61 | −123.7 | −7.4 | 25.1 | 9847.3 | 6006.9 |
| 24 | 17:50:52 | +01:31:45 | 27.29 | 14.16 | 51.0 | 36.0 | 0.64 | −116.9 | −19.1 | 31.1 | 731.6 | 446.3 |
| 25 | 17:43:01 | +13:53:39 | 38.08 | 21.32 | 20.4 | 36.0 | 0.46 | −117.6 | 8.8 | 21.9 | 462.7 | 282.3 |
| 26 | 17:46:50 | +03:50:40 | 28.94 | 16.11 | 24.0 | 27.0 | 0.82 | −117.0 | −14.7 | 23.6 | 370.0 | 225.7 |
| 27 | 17:37:02 | +01:34:28 | 25.66 | 17.23 | 9.0 | 15.0 | 0.48 | −116.4 | −25.4 | 21.0 | 95.3 | 58.1 |
| 28 | 17:50:28 | +14:24:37 | 39.37 | 19.88 | 98.8 | 69.0 | 1.03 | −115.5 | 15.7 | 34.5 | 4563.8 | 2783.9 |
| 29 | 17:34:37 | +08:52:18 | 32.26 | 21.07 | 14.8 | 21.0 | 0.30 | −117.3 | −7.7 | 22.9 | 118.6 | 72.4 |
| 30 | 18:04:43 | +11:14:24 | 37.87 | 15.40 | 41.2 | 75.0 | 0.80 | −113.3 | 16.9 | 27.1 | 1352.9 | 825.3 |
| 31 | 17:41:33 | +13:09:57 | 37.21 | 21.35 | 11.7 | 9.0 | 0.32 | −132.0 | −8.1 | 37.2 | 58.2 | 35.5 |
| | | | | | | | | −111.1 | 12.8 | 14.5 | 26.7 | 16.3 |
| 32 | 17:53:15 | +09:54:24 | 35.35 | 17.38 | 345.8 | 540.0 | 2.65 | −138.1 | −16.6 | 24.9 | 17260.0 | 10528.6 |
| | | | | | | | | −110.5 | 11.0 | 30.9 | 59575.7 | 36341.2 |
| 33 | 17:50:34 | +13:37:01 | 38.61 | 19.53 | 20.4 | 21.0 | 0.45 | −123.9 | 5.4 | 20.0 | 122.0 | 74.4 |
| | | | | | | | | −101.4 | 27.9 | 32.1 | 158.8 | 96.9 |
| 34 | 17:58:05 | +14:34:51 | 40.33 | 18.27 | 34.8 | 33.0 | 0.53 | −114.8 | 20.4 | 23.7 | 637.2 | 388.7 |
| 35 | 17:34:14 | +13:48:36 | 37.06 | 23.23 | 26.2 | 27.0 | 0.49 | −114.2 | 7.7 | 21.1 | 444.3 | 271.0 |
| 36 | 17:52:12 | +13:37:57 | 38.80 | 19.18 | 35.0 | 48.0 | 0.88 | −114.9 | 15.3 | 24.9 | 634.5 | 387.1 |
| 37 | 17:55:20 | +05:54:24 | 31.84 | 15.16 | 74.6 | 63.0 | 1.11 | −121.0 | −8.9 | 32.7 | 2890.3 | 1763.1 |
| | | | | | | | | −104.8 | 7.2 | 22.2 | 1239.4 | 756.0 |
| 38 | 17:54:45 | +07:09:09 | 32.94 | 15.84 | 8.9 | 18.0 | 0.30 | −109.6 | 5.5 | 40.9 | 129.8 | 79.1 |
| 39 | 17:25:35 | +09:30:07 | 31.83 | 23.36 | 53.3 | 81.0 | 0.62 | −105.4 | 1.2 | 32.7 | 2372.3 | 1447.1 |
| 40 | 17:49:49 | +02:33:54 | 28.12 | 14.86 | 45.0 | 51.0 | 0.38 | −106.8 | −6.6 | 41.1 | 1572.2 | 959.0 |
| 41 | 18:04:30 | +14:21:33 | 40.79 | 16.76 | 8.7 | 15.0 | 0.34 | −106.2 | 31.4 | 20.1 | 47.9 | 29.2 |
| 42 | 18:05:42 | +03:00:05 | 30.38 | 11.54 | 15.0 | 18.0 | 0.58 | −108.9 | 0.1 | 4.0 | 11.7 | 7.2 |
| | | | | | | | | −103.4 | 5.6 | 26.6 | 92.8 | 56.6 |

**Table 2**
(Continued)

| Cloud | R.A. (J2000) | Decl. (J2000) | $l$ (°) | $b$ (°) | ΔR.A.[a] (′) | ΔDecl.[a] (′) | $T_{b,\mathrm{peak}}$ (K) | $V_{\mathrm{LSR}}$ (km s$^{-1}$) | $V_{\mathrm{GSR}}$ (km s$^{-1}$) | $\Delta V$ (km s$^{-1}$) | $N_{\mathrm{H\,I}}$(tot) ($10^{18}$ cm$^{-2}$) | $M_{\mathrm{H\,I}}$[b] ($M_\odot$) |
|---|---|---|---|---|---|---|---|---|---|---|---|---|
| 43 | 17:35:44 | +02:54:30 | 26.74 | 18.14 | 62.9 | 246.0 | 0.67 | −104.7 | −10.6 | 27.4 | 7816.7 | 4768.2 |
| 44 | 17:32:56 | +01:25:43 | 25.02 | 18.07 | 30.0 | 18.0 | 0.95 | −104.3 | −15.9 | 22.7 | 402.2 | 245.3 |
| 45 | 18:03:07 | +08:22:54 | 35.02 | 14.52 | 14.8 | 9.0 | 0.31 | −99.1 | 23.1 | 34.4 | 96.0 | 58.5 |
| 46 | 17:29:25 | +08:35:43 | 31.39 | 22.11 | 50.4 | 24.0 | 0.35 | −102.7 | 3.5 | 26.3 | 541.4 | 330.2 |
| 47 | 18:04:28 | +08:04:14 | 34.89 | 14.08 | 14.9 | 21.0 | 0.37 | −98.1 | 24.0 | 26.0 | 148.6 | 90.7 |
| 48 | 17:57:52 | +11:48:43 | 37.66 | 17.16 | 14.7 | 21.0 | 0.30 | −110.9 | 17.6 | 28.5 | 139.1 | 84.9 |
| 49 | 17:41:33 | +09:40:26 | 33.82 | 19.88 | 23.7 | 30.0 | 0.30 | −97.1 | 18.1 | 24.3 | 222.7 | 135.8 |
| 50 | 17:26:14 | +12:28:43 | 34.86 | 24.47 | 14.7 | 18.0 | 0.34 | −97.0 | 17.5 | 23.9 | 98.3 | 60.0 |
| 51 | 17:46:02 | +07:13:51 | 32.01 | 17.81 | 23.8 | 24.0 | 0.30 | −95.9 | 15.2 | 26.2 | 227.6 | 138.8 |
| 52 | 18:09:16 | +06:37:59 | 34.10 | 12.38 | 17.9 | 24.0 | 0.42 | −95.9 | 24.6 | 20.9 | 225.8 | 137.8 |
| 53 | 17:43:29 | +11:33:41 | 35.86 | 20.25 | 8.8 | 24.0 | 0.37 | −94.6 | 26.3 | 30.2 | 190.3 | 116.1 |
| 54 | 17:51:31 | +03:45:19 | 29.41 | 15.04 | 9.0 | 12.0 | 0.31 | −95.3 | 9.0 | 16.0 | 38.2 | 23.3 |
| 55 | 17:45:53 | +04:12:46 | 29.17 | 16.49 | 23.9 | 45.0 | 0.53 | −96.4 | 6.4 | 39.3 | 1207.1 | 736.3 |
| 56 | 18:09:39 | +07:05:16 | 34.56 | 12.50 | 17.9 | 21.0 | 0.38 | −95.7 | 26.2 | 24.2 | 144.4 | 88.1 |
| 57 | 17:42:13 | +03:55:11 | 28.46 | 17.17 | 38.9 | 39.0 | 0.56 | −93.4 | 6.7 | 25.3 | 980.6 | 587.2 |
| 58 | 17:27:43 | +09:25:07 | 32.00 | 22.84 | 8.9 | 15.0 | 0.30 | −92.5 | 14.9 | 19.7 | 34.4 | 21.0 |
| 59 | 18:10:42 | +06:41:31 | 34.32 | 12.09 | 17.9 | 18.0 | 0.31 | −90.0 | 31.2 | 25.6 | 158.6 | 96.7 |
| 60 | 18:08:20 | +11:30:05 | 38.50 | 14.71 | 11.8 | 15.0 | 0.50 | −90.4 | 42.1 | 17.4 | 106.8 | 65.2 |
| 62 | 18:06:04 | +04:25:39 | 31.72 | 12.10 | 9.0 | 9.0 | 0.30 | −87.7 | 25.4 | 17.2 | 24.0 | 14.7 |
| 65 | 18:05:16 | +07:29:11 | 34.44 | 13.65 | 17.9 | 18.0 | 0.69 | −85.7 | 35.2 | 17.7 | 225.8 | 137.7 |
| 66 | 17:58:15 | +06:45:39 | 32.97 | 14.89 | 6.0 | 12.0 | 0.31 | −86.3 | 29.4 | 16.5 | 28.0 | 17.1 |
| 67 | 17:59:10 | +02:50:57 | 29.48 | 12.92 | 15.0 | 12.0 | 0.47 | −86.5<br>−74.5 | 19.0<br>31.0 | 14.5<br>69.6 | 91.5<br>96.0 | 55.8<br>58.5 |
| 68 | 17:49:49 | +04:33:20 | 29.95 | 15.78 | 12.0 | 48.0 | 0.33 | −84.8 | 20.9 | 22.9 | 241.2 | 147.1 |
| 69 | 17:29:29 | +09:47:39 | 32.57 | 22.62 | 5.9 | 6.0 | 0.31 | −91.0 | 18.3 | 24.5 | 25.7 | 15.7 |
| 70 | 17:41:24 | +10:53:06 | 34.97 | 20.43 | 23.6 | 21.0 | 0.31 | −82.8 | 35.3 | 24.6 | 177.2 | 108.1 |
| 71 | 18:06:09 | +11:39:44 | 38.42 | 15.26 | 11.8 | 9.0 | 0.30 | −84.4 | 47.5 | 28.8 | 101.1 | 61.7 |
| 72 | 18:00:12 | +03:28:21 | 30.17 | 12.97 | 18.0 | 21.0 | 0.30 | −80.1 | 27.6 | 25.1 | 181.0 | 110.4 |
| 73 | 18:01:02 | +04:22:56 | 31.10 | 13.20 | 9.0 | 12.0 | 0.34 | −81.4 | 29.2 | 18.1 | 55.4 | 33.8 |
| 74 | 18:01:39 | +07:58:18 | 34.48 | 14.66 | 11.9 | 27.0 | 0.43 | −79.2 | 41.3 | 22.7 | 191.4 | 116.7 |
| 75 | 18:03:44 | +07:50:30 | 34.59 | 14.15 | 14.9 | 12.0 | 0.31 | −78.5 | 42.6 | 23.7 | 110.2 | 67.2 |
| 77 | 18:02:07 | +03:36:21 | 30.51 | 12.61 | 15.0 | 15.0 | 0.34 | −77.2 | 31.8 | 27.4 | 128.5 | 78.4 |
| 80 | 17:36:30 | +01:31:18 | 25.54 | 17.33 | 30.0 | 27.0 | 0.38 | −74.1 | 16.5 | 27.7 | 253.0 | 154.3 |
| 81 | 18:04:27 | +07:15:38 | 34.14 | 13.73 | 17.9 | 18.0 | 0.53 | −76.3 | 43.6 | 20.4 | 176.1 | 107.4 |
| 84 | 18:00:57 | +05:13:15 | 31.86 | 13.60 | 56.8 | 111.0 | 0.70 | −70.9 | 41.9 | 26.6 | 1643.8 | 1002.7 |
| 87 | 17:46:25 | +04:38:56 | 29.64 | 16.57 | 15.0 | 27.0 | 0.39 | −69.1 | 35.2 | 29.0 | 242.4 | 147.9 |
| 88 | 17:56:59 | +10:12:34 | 36.05 | 16.68 | 44.3 | 45.0 | 2.23 | −70.5<br>−66.6 | 53.5<br>57.4 | 33.2<br>11.1 | 985.6<br>756.7 | 601.2<br>461.6 |
| 89 | 17:34:13 | +11:03:10 | 34.34 | 22.10 | 64.8 | 111.0 | 0.51 | −65.6 | 49.4 | 40.0 | 3603.7 | 2198.3 |
| 90 | 18:03:41 | +13:50:53 | 40.22 | 16.73 | 14.6 | 12.0 | 0.33 | −68.2 | 67.9 | 21.5 | 49.1 | 29.9 |

**Notes.**
[a] At the distance of 10 kpc, $1' = 2.9$ pc.
[b] At the distance of 10 kpc.

**Table 3**
Catalog of Clouds in the Complex C Data with $-65 < V_{LSR} < -50$km s$^{-1}$

| Cloud | R.A. (J2000) | Decl. (J2000) | $l$ (°) | $b$ (°) | ΔR.A.[a] (′) | ΔDecl.[a] (′) | $T_{b,peak}$ (K) | $V_{LSR}$ (km s$^{-1}$) | $V_{GSR}$ (km s$^{-1}$) | $\Delta V$ (km s$^{-1}$) | $N_{HI}$(tot) ($10^{18}$ cm$^{-2}$) | $M_{HI}$[b] ($M_\odot$) |
|---|---|---|---|---|---|---|---|---|---|---|---|---|
| 91 | 18:08:03 | +03:59:08 | 31.55 | 11.46 | 21.0 | 21.0 | 0.45 | −63.7 | 49.1 | 29.8 | 274.4 | 167.4 |
| 94 | 17:53:28 | +14:31:47 | 39.80 | 19.27 | 43.6 | 48.0 | 0.55 | −62.3 | 70.6 | 29.6 | 1769.6 | 1079.5 |
| 98 | 17:58:41 | +11:18:22 | 37.27 | 16.77 | 11.8 | 24.0 | 0.36 | −59.9 | 67.6 | 26.7 | 171.4 | 104.5 |
| 101 | 17:46:21 | +08:34:07 | 33.31 | 18.33 | 14.8 | 21.0 | 0.30 | −59.8 | 54.9 | 24.4 | 109.8 | 67.0 |
| 104 | 17:58:52 | +14:12:25 | 40.05 | 17.94 | 26.2 | 36.0 | 0.42 | −61.4 | 73.3 | 19.5 | 405.4 | 247.3 |
| | | | | | | | | −53.0 | 81.7 | 4.7 | 21.0 | 12.8 |
| 106 | 18:04:33 | +06:30:35 | 33.45 | 13.37 | 47.7 | 60.0 | 0.78 | −59.6 | 58.4 | 24.9 | 1113.8 | 679.4 |
| 108 | 17:41:04 | +06:42:11 | 30.94 | 18.69 | 56.6 | 51.0 | 0.68 | −58.9 | 48.2 | 31.1 | 1711.4 | 1044.0 |
| 109 | 18:02:30 | +14:19:41 | 40.55 | 17.19 | 26.2 | 39.0 | 0.36 | −59.4 | 77.3 | 27.8 | 603.3 | 368.0 |
| 110 | 18:07:13 | +12:55:02 | 39.71 | 15.56 | 11.7 | 12.0 | 0.44 | −59.8 | 75.6 | 22.9 | 99.6 | 60.8 |
| 111 | 17:47:40 | +03:46:08 | 28.97 | 15.89 | 26.9 | 27.0 | 0.57 | −61.1 | 41.4 | 19.0 | 164.0 | 100.1 |
| | | | | | | | | −54.7 | 47.8 | 7.1 | 45.5 | 27.7 |
| 112 | 18:10:17 | +11:04:13 | 38.32 | 14.09 | 35.3 | 84.0 | 2.85 | −60.7 | 71.6 | 12.0 | 869.3 | 530.3 |
| 114 | 17:49:47 | +14:38:05 | 39.51 | 20.12 | 34.8 | 21.0 | 0.41 | −57.6 | 73.9 | 20.3 | 335.8 | 204.8 |
| 117 | 17:20:45 | +12:16:24 | 34.04 | 25.60 | 8.8 | 9.0 | 0.35 | −57.6 | 53.5 | 24.9 | 58.6 | 35.8 |

**Notes.**
[a] t the distance of 10 kpc, $1' = 2.9$ pc.
[b] At the distance of 10 kpc.

*Column 13*. H I mass (in $M_\odot$), assuming that all observed Complex C clouds are 10 kpc away (Thom et al. 2008) as described in Section 4.

Table 2 ($V_{LSR} < -65$ km s$^{-1}$) contains 79 clouds. If two Gaussians are required to fit the total spectrum of a cloud, the two Gaussians will be listed separately in the catalog. The two rows will share the same position and size information (Columns 1–7), but have different velocities, H I column densities and masses (Columns 8–12). The clouds between $V_{LSR} = -65$ and $-50$ km s$^{-1}$ are included in a separate catalog containing 14 clouds (Table 3). This separate catalog was created because we found a break in the velocity distribution of the clouds at approximately $-65$ km s$^{-1}$, indicating this is a natural cutoff point for clouds that are clearly associated with Complex C. The clouds of Table 3 are also not included in the statistics discussed in Section 4.

In the smoothed Complex C cube, the number of detected clouds is much smaller (16) because small discrete clouds are often merged into larger clouds. Table 4 shows the catalog of clouds created from the smoothed cube, where we exclude the clouds that have a $V_{LSR}$ between $-65$ and $-50$ km s$^{-1}$.

### 3.3. Magellanic Stream Cloud Catalog

The Magellanic Stream data have different noise levels in the two spatial regions considered here due to differing integration times (see S08). The statistics are determined separately for these two regions: for region 1 we used a detection threshold of 0.27 K ($5\sigma$) and a grow parameter of 0.17 K ($3\sigma$); for region 2 we used a detection threshold of 0.15 K ($5\sigma$) and a grow parameter of 0.09 K ($3\sigma$). We searched the cubes from $-420$ to $-280$ km s$^{-1}$, where there is evident Stream emission. The search parameters are tabulated in Table 1. Figure 5 shows the integrated intensity maps of the Duchamp detections for regions 1 and 2.

The Stream cubes are plagued with more RFI than the Complex C cube. We excluded 62% of the clouds found by Duchamp in region 1 and 31% of the clouds in region 2 due to RFI artifacts or overlap of the two regions. Figure 7 shows the integrated intensity map of the real cloud detections and Table 5 contains the catalog of clouds found in the Magellanic Stream data. The entries are the same as those in Table 2 with the exception of the H I mass being calculated at a distance of 60 kpc. Also, at the distance of 60 kpc, the conversion between angular size and physical size is given by $1' = 17$ pc. These relationships can be easily scaled to other distances using $M_{HI}$(d (kpc)) $= M_{HI}(60\,\mathrm{kpc})(\mathrm{d}/60\,\mathrm{kpc})^2$ and size(60 kpc)(d/60 kpc) or 17 pc × size(′)(d/60 kpc).

## 4. RESULTS

In this section, we present the distributions of cloud properties and, given we have distance constraints for Complex C and the Magellanic Stream, derive the physical properties of the clouds. A summary of the cloud properties is found in Table 6. The physical properties are derived using the following methods.

1. The mass of a cloud is derived at the distance of 10 kpc in the case of Complex C and 60 kpc for the Magellanic Stream from the total column density of the cloud using, $M_{HI}(M_\odot) = 5.5 \times 10^{-21}\ N_{HI}(\mathrm{tot}) \times \mathrm{d(kpc)}^2$.
2. The angular size of a cloud is given by $\sqrt{\Delta\mathrm{R.A.}\ \Delta\mathrm{decl.}}$, and the physical size = 0.291 × angularsize× d(kpc).
3. The volume density ($n_c$) of a cloud is calculated by assuming that the clouds are spherical, with the radius $R = \sqrt{\Delta\mathrm{R.A.}\ \Delta\mathrm{decl.}}/2$. Clouds with aspect ratios greater than 1.6 are excluded from this calculation.
4. The cloud pressure is given by $P_c = kn_cT_c$, where we assume the warm neutral component is at 9000 K.

### 4.1. Complex C

#### 4.1.1. The Original Complex C Cube

Seventy-nine clouds were cataloged in the searched region of the Complex C cube at $V_{LSR} < -65$ km s$^{-1}$, and 14 were

**Table 4**
Smoothed Complex C Cloud Catalog

| Cloud | R.A. (J2000) | Decl. (J2000) | $l$ (°) | $b$ (°) | ΔR.A.[a] (′) | ΔDecl.[a] (′) | $T_{b,\mathrm{peak}}$ (K) | $V_{\mathrm{LSR}}$ (km s$^{-1}$) | $V_{\mathrm{GSR}}$ (km s$^{-1}$) | $\Delta V$ (km s$^{-1}$) | $N_{\mathrm{H\,I}}$(tot) ($10^{18}$ cm$^{-2}$) | $M_{\mathrm{H\,I}}$[b] ($M_\odot$) |
|---|---|---|---|---|---|---|---|---|---|---|---|---|
| 1 | 17:57:33 | +08:50:39 | 34.83 | 15.96 | 41.5 | 63.0 | 0.16 | −130.4 | −9.6 | 36.4 | 1523.4 | 929.2 |
| 2 | 17:33:05 | +12:29:59 | 35.63 | 22.95 | 26.4 | 42.0 | 0.14 | −126.2 | −8.2 | 22.3 | 312.0 | 190.3 |
| 3 | 17:51:04 | +01:28:43 | 27.27 | 14.09 | 33.0 | 24.0 | 0.18 | −120.4 | −22.6 | 26.2 | 328.6 | 200.5 |
| 4 | 17:28:24 | +08:02:01 | 30.73 | 22.09 | 29.7 | 33.0 | 0.15 | −119.9 | −15.7 | 26.0 | 478.3 | 291.7 |
| 5 | 17:54:13 | +07:26:50 | 33.15 | 16.09 | 59.5 | 45.0 | 0.32 | −119.2 | −3.6 | 26.0 | 840.0 | 512.4 |
| | | | | | | | | −119.5 | −4.0 | 5.9 | 92.0 | 56.1 |
| 6 | 17:42:54 | +13:53:17 | 38.06 | 21.34 | 29.1 | 45.0 | 0.17 | −116.3 | 10.0 | 23.4 | 581.6 | 354.8 |
| 7 | 17:34:13 | +13:50:47 | 37.09 | 23.25 | 26.2 | 36.0 | 0.17 | −114.2 | 7.7 | 21.9 | 437.5 | 266.8 |
| 8 | 17:49:53 | +02:35:52 | 28.15 | 14.87 | 53.9 | 72.0 | 0.17 | −106.7 | −6.3 | 44.1 | 1997.3 | 1218.4 |
| 9 | 17:25:38 | +09:33:24 | 31.89 | 23.37 | 56.2 | 78.0 | 0.23 | −105.0 | 1.7 | 33.5 | 2485.2 | 1516.0 |
| 10 | 17:35:24 | +02:52:32 | 26.67 | 18.20 | 116.9 | 249.0 | 0.37 | −105.1 | −11.3 | 28.5 | 9516.7 | 5805.2 |
| 11 | 17:38:14 | +10:48:51 | 34.55 | 21.10 | 170.9 | 255.0 | 0.81 | −124.1 | −7.7 | 26.9 | 15145.5 | 9238.8 |
| 12 | 17:55:11 | +09:34:30 | 35.25 | 16.80 | 434.9 | 633.0 | 1.08 | −113.0 | 8.6 | 45.0 | 117964.9 | 71958.6 |
| 13 | 17:42:23 | +03:54:32 | 28.47 | 17.13 | 38.9 | 45.0 | 0.21 | −94.6 | 5.7 | 24.9 | 903.7 | 551.2 |
| 14 | 17:46:08 | +02:39:50 | 27.77 | 15.73 | 42.0 | 45.0 | 0.14 | −95.4 | 3.3 | 27.0 | 671.3 | 4009.5 |
| 15 | 18:04:59 | +07:28:14 | 34.39 | 13.70 | 29.8 | 36.0 | 0.14 | −84.2 | 36.6 | 19.1 | 244.7 | 149.3 |
| 16 | 18:00:37 | +04:55:21 | 31.54 | 13.54 | 53.8 | 111.0 | 0.20 | −80.7 | 31.2 | 21.3 | 1007.3 | 614.4 |
| | | | | | | | | −67.7 | 9.0 | 13.3 | 381.6 | 232.8 |

**Notes.**
[a] At the distance of 10 kpc, $1' = 2.9$ pc.
[b] At the distance of 10 kpc.

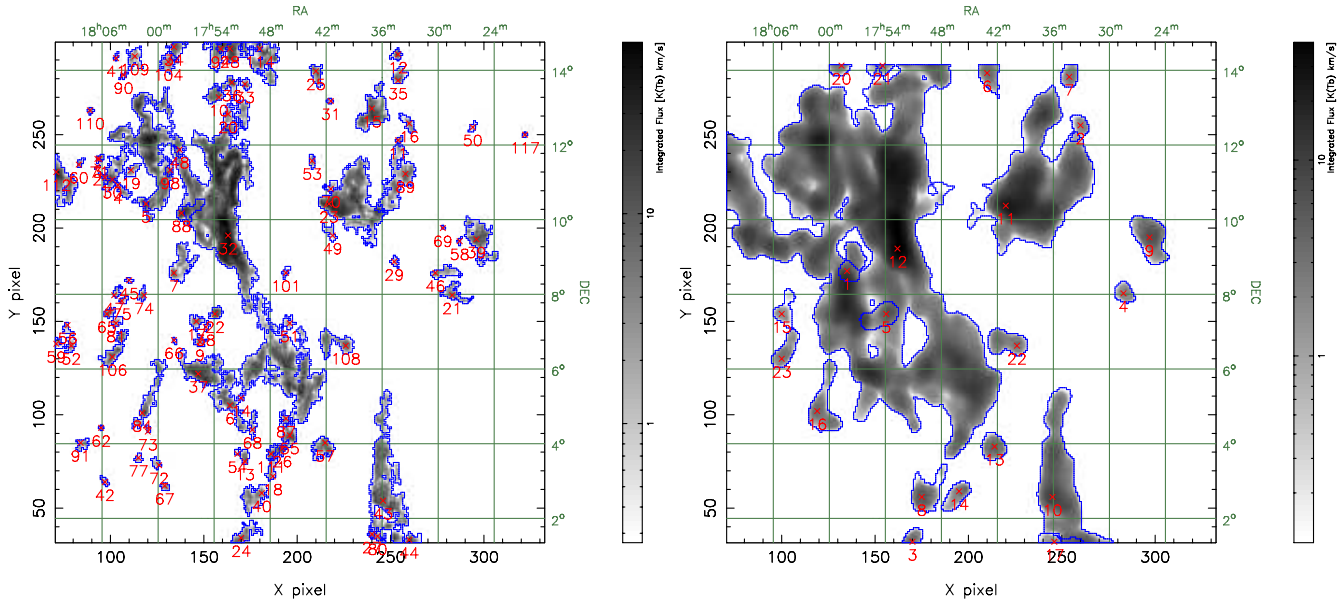


**Figure 4.** Intensity maps of the detections in the Complex C data cube as provided by Duchamp. Note that some numbers are missing as they are excluded from the catalog (see Section 3.1). The left map has the original spatial resolution of 3.′4. Clouds 1–90 are included in Table 2, and clouds 91–117 have $V_{\mathrm{LSR}} > -65$km s$^{-1}$ and are included in Table 3. The right map is spatially smoothed to 18′ before the clouds are cataloged. Clouds 1–16 are cataloged in Table 4, and clouds 17–23 have $V_{\mathrm{LSR}} > -65$km s$^{-1}$ and are not cataloged.
(A color version of this figure is available in the online journal.)

cataloged at $-65 < V_{\mathrm{LSR}} < -50$ km s$^{-1}$. Traditionally HVCs such as Complex C are defined to have $V_{\mathrm{LSR}} \lesssim -90$ km s$^{-1}$, but from the distribution of clouds in the data cube, there is no distinct cutoff at this velocity. There is however, a minimum number of clouds around $-65$ km s$^{-1}$, and the channel maps also show a transition from Complex C to a separate, intermediate velocity population around this velocity. Thus in this analysis we only include the clouds with $V_{\mathrm{LSR}} < -65$ km s$^{-1}$. We inspected the clouds at $-65 < V_{\mathrm{LSR}} < -50$ km s$^{-1}$, and found that the overall statistics we present here would not change significantly

**Table 5**
Magellanic Stream Cloud Catalog

| Cloud | R.A. (J2000) | Decl. (J2000) | $l$ (°) | $b$ (°) | ΔR.A.[a] (′) | ΔDecl.[a] (′) | $T_{b,\mathrm{peak}}$ (K) | $V_{\mathrm{LSR}}$ (km s$^{-1}$) | $V_{\mathrm{GSR}}$ (km s$^{-1}$) | $\Delta V$ (km s$^{-1}$) | $N_{\mathrm{H\,I}}$(tot) ($10^{18}$ cm$^{-2}$) | $M_{\mathrm{H\,I}}$[b] $M_{\odot}$ |
|---|---|---|---|---|---|---|---|---|---|---|---|---|
| 2 | 22:23:33 | +20:26:16 | 82.10 | −30.47 | 14.1 | 21.0 | 0.39 | −411.0 | −223.1 | 18.5 | 84.4 | 1852.9 |
| 5 | 22:08:53 | +17:15:38 | 76.64 | −30.64 | 25.8 | 24.0 | 0.34 | −407.8 | −223.7 | 25.5 | 200.0 | 4391.0 |
| 7 | 22:19:13 | +21:04:50 | 81.65 | −29.33 | 33.6 | 27.0 | 0.34 | −406.5 | −216.7 | 20.7 | 223.8 | 4914.4 |
| 8 | 22:42:31 | +18:41:13 | 85.10 | −34.55 | 25.6 | 18.0 | 0.28 | −407.2 | −226.7 | 26.2 | 180.4 | 3962.0 |
| 9 | 23:25:38 | +18:41:18 | 96.18 | −39.69 | 17.1 | 24.0 | 0.28 | −404.5 | −236.2 | 19.5 | 119.0 | 2612.9 |
| 11 | 22:24:20 | +20:05:59 | 82.02 | −30.85 | 19.7 | 30.0 | 0.52 | −403.7 | −216.6 | 23.6 | 384.9 | 8451.6 |
| 13 | 22:17:21 | +21:10:09 | 81.33 | −28.99 | 11.2 | 15.0 | 0.30 | −400.9 | −210.7 | 25.1 | 57.9 | 1270.8 |
| 14 | 22:40:05 | +17:10:27 | 83.45 | −35.44 | 11.5 | 15.0 | 0.35 | −399.7 | −221.6 | 61.1 | 120.0 | 2636.5 |
| | | | | | | | | −401.8 | −223.7 | 9.2 | 20.8 | 456.8 |
| 15 | 23:04:18 | +20:35:35 | 91.64 | −35.69 | 42.1 | 57.0 | 0.84 | −402.5 | −223.9 | 38.6 | 1971.7 | 43297.7 |
| 17 | 22:30:03 | +19:22:30 | 82.75 | −32.25 | 8.5 | 9.0 | 0.28 | −401.2 | −216.6 | 28.0 | 36.4 | 799.2 |
| 18 | 23:00:03 | +17:17:34 | 88.46 | −38.01 | 14.3 | 18.0 | 0.30 | −396.8 | −223.5 | 25.9 | 89.0 | 1954.8 |
| 19 | 22:26:05 | +17:37:57 | 80.59 | −33.03 | 22.9 | 33.0 | 0.28 | −401.3 | −219.3 | 30.0 | 209.0 | 4589.1 |
| 20 | 22:29:32 | +17:04:13 | 80.93 | −33.99 | 22.9 | 18.0 | 0.37 | −395.7 | −215.6 | 29.5 | 261.6 | 5744.5 |
| 21 | 22:44:44 | +18:44:06 | 85.66 | −34.81 | 22.7 | 33.0 | 0.33 | −391.6 | −211.5 | 44.8 | 458.0 | 10058.1 |
| 22 | 22:45:27 | +21:08:44 | 87.46 | −32.91 | 14.0 | 24.0 | 0.36 | −389.6 | −205.1 | 30.5 | 96.7 | 2122.6 |
| 28 | 22:44:39 | +21:18:30 | 87.38 | −32.67 | 11.2 | 12.0 | 0.30 | −385.9 | −200.9 | 25.6 | 36.6 | 804.0 |
| 29 | 22:14:14 | +21:44:48 | 81.11 | −28.08 | 5.6 | 6.0 | 0.31 | −384.9 | −193.1 | 9.3 | 9.8 | 215.4 |
| 31 | 22:14:41 | +20:50:40 | 80.55 | −28.84 | 14.0 | 15.0 | 0.29 | −385.1 | −195.0 | 31.5 | 102.9 | 2260.4 |
| 33 | 23:10:07 | +19:13:22 | 92.30 | −37.55 | 39.7 | 27.0 | 0.78 | −381.6 | −207.3 | 20.4 | 448.1 | 9839.6 |
| 34 | 22:30:32 | +18:24:46 | 82.16 | −33.08 | 17.1 | 12.0 | 0.32 | −382.1 | −199.5 | 20.4 | 63.4 | 1391.6 |
| 38 | 23:13:56 | +16:20:22 | 91.54 | −40.52 | 11.5 | 12.0 | 0.27 | −376.0 | −208.8 | 24.9 | 64.0 | 1404.7 |
| 39 | 22:57:09 | +16:55:47 | 87.47 | −37.95 | 23.0 | 15.0 | 0.39 | −376.4 | −203.1 | 26.4 | 195.2 | 4286.5 |
| 43 | 22:37:10 | +17:47:25 | 83.21 | −34.53 | 20.0 | 18.0 | 0.29 | −372.8 | −192.8 | 22.4 | 65.1 | 1428.5 |
| 44 | 22:44:35 | +19:10:48 | 85.93 | −34.42 | 14.2 | 15.0 | 0.29 | −378.1 | −197.1 | 23.1 | 58.2 | 1277.2 |
| 45 | 22:29:42 | +16:37:00 | 80.63 | −34.37 | 25.9 | 21.0 | 0.31 | −371.0 | −191.9 | 27.7 | 230.8 | 5067.5 |
| 47 | 22:51:11 | +18:38:14 | 87.14 | −35.74 | 14.2 | 18.0 | 0.52 | −369.5 | −191.1 | 27.8 | 157.7 | 3463.4 |
| 48 | 22:47:14 | +18:57:50 | 86.41 | −34.95 | 8.5 | 12.0 | 0.34 | −367.2 | −187.2 | 17.6 | 28.6 | 627.1 |
| 51 | 23:14:49 | +17:29:52 | 92.50 | −39.60 | 77.3 | 54.0 | 0.48 | −362.6 | −193.2 | 34.9 | 2131.7 | 46811.1 |
| 52 | 23:03:57 | +16:35:43 | 89.01 | −39.09 | 31.6 | 27.0 | 0.63 | −358.8 | −188.1 | 30.4 | 559.8 | 12292.4 |
| 54 | 22:41:26 | +16:25:22 | 83.22 | −36.23 | 25.9 | 15.0 | 0.44 | −357.9 | −181.7 | 25.1 | 215.5 | 4731.6 |
| 57 | 23:25:00 | +17:00:53 | 95.06 | −41.13 | 14.3 | 18.0 | 0.43 | −353.6 | −188.6 | 22.2 | 143.2 | 3144.2 |
| 59 | 23:15:25 | +16:31:48 | 92.07 | −40.52 | 28.8 | 27.0 | 0.48 | −345.8 | −178.7 | 38.3 | 458.7 | 10073.3 |
| 67 | 23:14:11 | +16:52:08 | 91.94 | −40.08 | 20.1 | 21.0 | 0.31 | −333.2 | −165.0 | 28.9 | 188.0 | 4129.3 |
| 76 | 21:59:51 | +20:46:43 | 77.55 | −26.60 | 36.5 | 54.0 | 0.48 | −307.1 | −115.0 | 27.0 | 1015.4 | 22298.1 |
| 2 | 23:49:08 | +11:45:24 | 99.67 | −48.28 | 17.6 | 12.0 | 0.25 | −391.0 | −246.7 | 37.1 | 157.1 | 3449.2 |
| 3 | 22:49:24 | +14:15:31 | 83.58 | −39.11 | 81.4 | 105.0 | 0.41 | −387.5 | −217.8 | 41.6 | 3849.9 | 84543.9 |
| 4 | 22:46:28 | +15:04:24 | 83.45 | −38.04 | 8.7 | 15.0 | 0.18 | −375.4 | −203.3 | 39.2 | 62.7 | 1376.7 |
| | | | | | | | | −351.6 | −179.5 | 21.3 | 20.3 | 445.7 |
| 6 | 22:58:46 | +14:51:49 | 86.44 | −39.89 | 29.0 | 18.0 | 0.16 | −367.9 | −199.5 | 50.9 | 182.1 | 3999.9 |
| | | | | | | | | −376.7 | −208.3 | 15.7 | 23.8 | 523.4 |
| 7 | 23:06:39 | +12:43:00 | 87.04 | −42.74 | 125.8 | 225.0 | 0.60 | −375.1 | −213.7 | 45.0 | 12175.2 | 267368.4 |
| 8 | 22:52:57 | +12:22:29 | 83.06 | −41.15 | 61.5 | 93.0 | 0.38 | −373.3 | −208.8 | 33.0 | 2684.2 | 58944.7 |
| 9 | 22:53:25 | +13:13:17 | 83.83 | −40.52 | 20.4 | 24.0 | 0.23 | −372.9 | −206.6 | 30.7 | 140.3 | 3081.5 |
| 10 | 23:06:41 | +15:20:24 | 88.89 | −40.51 | 37.6 | 27.0 | 0.21 | −372.2 | −205.0 | 34.0 | 421.9 | 9264.1 |
| 11 | 23:02:06 | +15:37:08 | 87.85 | −39.69 | 14.5 | 12.0 | 0.16 | −366.8 | −197.6 | 29.4 | 53.6 | 1177.6 |

**Table 5**
(Continued)

| Cloud | R.A. (J2000) | Decl. (J2000) | $l$ (°) | $b$ (°) | ΔR.A.[a] (′) | ΔDecl.[a] (′) | $T_{b,\mathrm{peak}}$ (K) | $V_{\mathrm{LSR}}$ (km s$^{-1}$) | $V_{\mathrm{GSR}}$ (km s$^{-1}$) | $\Delta V$ (km s$^{-1}$) | $N_{\mathrm{H\,I}}$(tot) ($10^{18}$ cm$^{-2}$) | $M_{\mathrm{H\,I}}$[b] $M_{\odot}$ |
|---|---|---|---|---|---|---|---|---|---|---|---|---|
| 12 | 22:31:07 | +15:54:39 | 80.42 | −35.13 | 20.2 | 15.0 | 0.20 | −364.6 | −187.1 | 27.6 | 100.1 | 2198.7 |
| 13 | 23:03:15 | +13:14:02 | 86.47 | −41.85 | 58.4 | 72.0 | 0.26 | −362.2 | −198.6 | 31.6 | 879.1 | 19304.8 |
| 14 | 23:45:14 | +14:53:51 | 100.02 | −45.01 | 11.6 | 27.0 | 0.16 | −357.5 | −204.3 | 31.3 | 68.4 | 1501.0 |
| 15 | 22:46:25 | +15:25:13 | 83.70 | −37.75 | 31.8 | 51.0 | 0.24 | −359.1 | −186.2 | 31.7 | 519.2 | 11401.1 |
| 16 | 22:55:41 | +15:09:05 | 85.84 | −39.24 | 20.3 | 21.0 | 0.16 | −357.2 | −187.2 | 25.6 | 110.6 | 2429.7 |
| 17 | 23:35:14 | +14:15:21 | 96.52 | −44.67 | 20.4 | 15.0 | 0.21 | −356.6 | −201.2 | 24.8 | 126.1 | 2768.8 |
| 18 | 22:37:07 | +14:08:33 | 80.46 | −37.42 | 20.4 | 21.0 | 0.38 | −355.3 | −182.9 | 24.2 | 183.0 | 4018.8 |
| 19 | 23:34:07 | +13:06:13 | 95.49 | −45.61 | 35.1 | 21.0 | 0.32 | −353.9 | −200.7 | 28.3 | 269.8 | 5924.8 |
| 21 | 23:00:10 | +14:20:36 | 86.44 | −40.51 | 23.3 | 33.0 | 0.36 | −355.5 | −188.6 | 29.0 | 380.7 | 8359.3 |
| 22 | 22:25:12 | +14:42:57 | 78.14 | −35.14 | 20.3 | 24.0 | 0.19 | −353.2 | −177.1 | 23.6 | 185.4 | 4070.6 |
| 23 | 23:21:19 | +13:04:41 | 91.54 | −44.23 | 14.6 | 15.0 | 0.16 | −354.4 | −196.8 | 27.3 | 62.2 | 1366.5 |
| 24 | 23:44:47 | +12:19:33 | 98.50 | −47.36 | 11.7 | 9.0 | 0.16 | −353.8 | −206.4 | 22.3 | 31.8 | 699.1 |
| 25 | 23:45:38 | +15:21:27 | 100.38 | −44.61 | 20.3 | 39.0 | 0.29 | −351.9 | −197.9 | 24.8 | 240.3 | 5276.8 |
| 26 | 23:12:55 | +14:04:30 | 89.77 | −42.36 | 122.2 | 111.0 | 0.48 | −352.0 | −189.5 | 44.5 | 3624.9 | 79603.2 |
| 27 | 23:33:27 | +12:42:45 | 95.05 | −45.89 | 41.0 | 24.0 | 0.19 | −349.8 | −197.2 | 32.1 | 248.5 | 5456.9 |
| 29 | 22:55:56 | +13:41:37 | 84.85 | −40.49 | 14.6 | 15.0 | 0.26 | −349.8 | −183.1 | 22.9 | 83.1 | 1824.3 |
| 30 | 23:01:40 | +12:35:50 | 85.57 | −42.18 | 41.0 | 27.0 | 0.35 | −352.3 | −189.8 | 41.1 | 464.0 | 10188.5 |
| 31 | 23:36:31 | +12:45:56 | 96.05 | −46.16 | 11.7 | 12.0 | 0.21 | −351.2 | −199.6 | 25.8 | 41.0 | 900.8 |
| 33 | 23:02:18 | +11:48:05 | 85.14 | −42.92 | 35.2 | 18.0 | 0.38 | −349.0 | −188.5 | 24.9 | 364.3 | 8000.0 |
| 34 | 23:11:40 | +12:58:50 | 88.65 | −43.15 | 23.4 | 24.0 | 0.42 | −346.6 | −186.2 | 20.2 | 184.1 | 4043.6 |
| 35 | 23:25:26 | +14:05:38 | 93.43 | −43.80 | 87.3 | 78.0 | 0.29 | −346.3 | −187.8 | 31.8 | 1487.7 | 32699.9 |
| 37 | 22:58:00 | +12:22:12 | 84.40 | −41.86 | 29.3 | 24.0 | 0.17 | −341.4 | −178.3 | 27.0 | 158.1 | 3471.8 |
| 38 | 23:26:30 | +12:12:48 | 92.55 | −45.59 | 202.3 | 102.0 | 0.65 | −341.4 | −187.6 | 30.3 | 6359.7 | 139659.1 |
| 43 | 22:38:41 | +13:54:50 | 80.66 | −37.83 | 20.4 | 27.0 | 0.22 | −339.2 | −167.7 | 34.9 | 253.9 | 5576.4 |
| 49 | 22:33:25 | +13:17:41 | 78.91 | −37.51 | 55.5 | 39.0 | 0.26 | −328.2 | −156.9 | 27.7 | 964.1 | 21172.5 |
| 50 | 22:38:01 | +14:31:34 | 80.97 | −37.25 | 29.0 | 21.0 | 0.20 | −328.3 | −155.3 | 28.0 | 221.7 | 4868.3 |
| 51 | 23:17:54 | +14:50:37 | 91.70 | −42.28 | 17.4 | 27.0 | 0.18 | −328.1 | −165.4 | 23.0 | 81.3 | 1785.8 |
| 52 | 23:14:08 | +12:31:55 | 89.05 | −43.85 | 26.4 | 27.0 | 0.17 | −325.8<br>−338.4 | −167.2<br>−179.8 | 16.9<br>46.3 | 59.7<br>123.4 | 1310.5<br>2710.3 |
| 53 | 22:34:00 | +12:17:06 | 78.23 | −38.38 | 17.6 | 12.0 | 0.17 | −321.3 | −152.5 | 21.5 | 39.7 | 872.8 |

**Notes.**
[a] At the distance of 60 kpc, $1' = 17$ pc.
[b] At the distance of 60 kpc.

if we included these clouds. They are included in Table 3 for those interested in that set of clouds.

Figure 6 shows the peak $T_b$, central velocity, line width, and angular size for the 79 clouds cataloged. The distance dependent properties of the clouds are shown in Figures 8 and 13 with the exception of the physical size of the clouds at 10 kpc, which for ease of presentation we show as the top axis on the angular size distribution plot. Most of the clouds have a peak $T_b$ under 1 K with a few exceptions. The cutoff at 0.29 K is determined by the noise level of the cube and the cataloging parameters, and there is no evidence for a turnover before this value, which suggests that the cloud number continues to increase below our detection limit. The line width histogram shows that the cloud line width distribution peaks between 20 and 30 km s$^{-1}$, 67% of the clouds are found within this peak. The median line width is 24.9 km s$^{-1}$. Eight of the clouds required a double Gaussian to fit to their line profiles. The solid lines in the line width and central velocity plots show only the clouds that were fit with a single Gaussian, while the dashed lines include the clouds fit with either one or two Gaussians, treating the two components as two separate clouds.

The velocity distribution of the clouds extends from −178 to −64 km s$^{-1}$ (LSR; 41–84 km s$^{-1}$ in the GSR frame), with the upper cutoff described above. The distribution has a peak at −120 km s$^{-1}$, but it is not very pronounced. There is a steady decline in the number of clouds as one approaches less negative velocities. The sizes of the clouds are shown in both arc minutes and the corresponding physical size at 10 kpc. Sixty-six percent

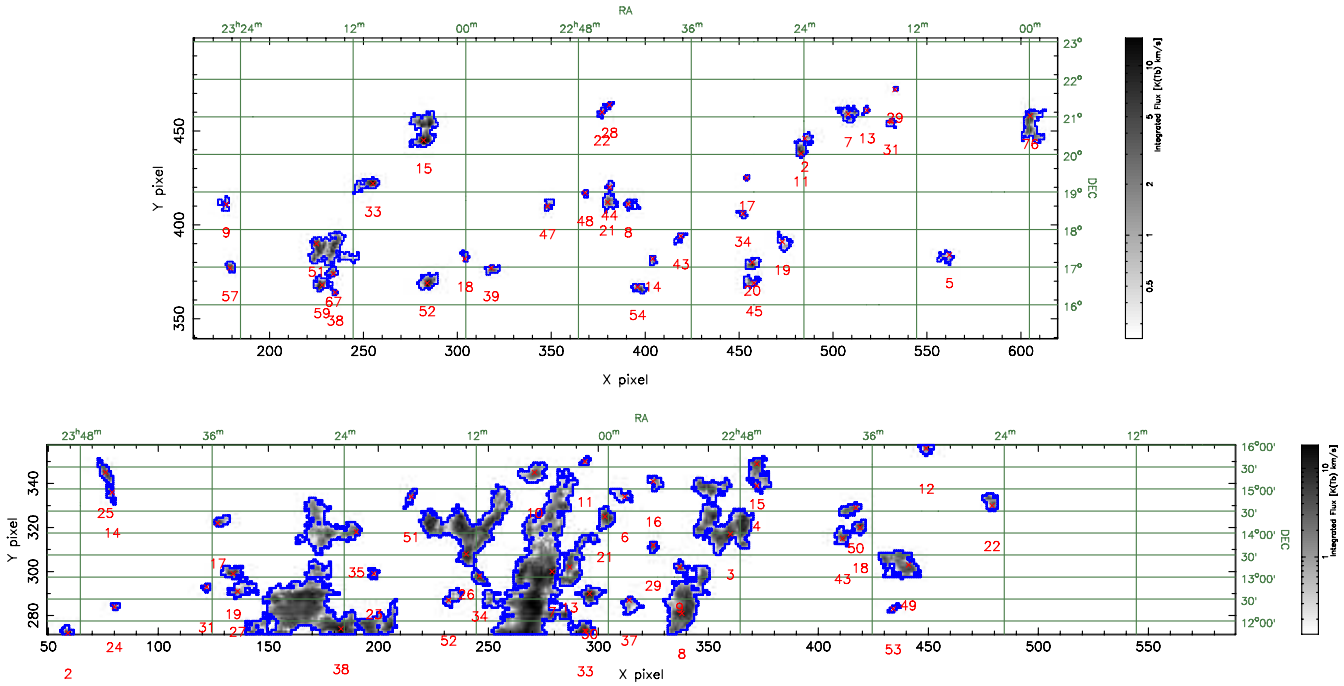


**Figure 5.** Integrated intensity map of the detections in two regions at the tail of the Magellanic Stream as provided by Duchamp (top corresponds to "region 1" and bottom corresponds to "region 2"). See Table 5 for the data on each numbered cloud.

(A color version of this figure is available in the online journal.)

**Table 6**
Mean and Median Values of the Cloud Statistics

| Property | Unit | Complex C | | Smoothed C | | Magellanic Stream | |
|---|---|---|---|---|---|---|---|
| Number of clouds[a] | | 79 | | 16 | | 72 | |
| Clouds with single component[b] | | 71 | | 14 | | 68 | |
| Single comp. clouds w/aspect ratio <1.6[c] | | 54 | | 13 | | 59 | |
| Adopted distance | kpc | 10 | | 10 | | 60 | |
| Velocity range of catalog | km s$^{-1}$ | −178 to −66 | | −130 to −80 | | −411 to −307 | |
| | | Mean | Median | Mean | Median | Mean | Median |
| $T_{b,peak}$[a] | K | 0.56 | 0.41 | 0.42 | 0.18 | 0.33 | 0.30 |
| $\Delta V$[a] | km s$^{-1}$ | 26.3 | 24.9 | 28.2 | 26.2 | 29.3 | 27.7 |
| $V_{LSR}$[a] | km s$^{-1}$ | −107 | −105 | −110 | −113 | −367 | −364 |
| Mass[a] | $M_\odot$ | 1300 | 148 | 6560 | 632 | 16400 | 4520 |
| Size[a] | ′ | 35.1 | 22.2 | 90.0 | 51.7 | 30.4 | 22.1 |
| Size[a] | pc | 102 | 64.4 | 261 | 150 | 517 | 376 |
| Volume density[c] | cm$^{-3}$ | 0.079 | 0.064 | | [d] | 0.010 | 0.0093 |
| Pressure ($P/k$)[c] | K cm$^{-3}$ | 710 | 580 | | [d] | 91 | 84 |
| Halo density[c] | cm$^{-3}$ | $7.1 \times 10^{-4}$ | $5.8 \times 10^{-4}$ | | [d] | $9.1 \times 10^{-5}$ | $8.4 \times 10^{-5}$ |

**Notes.**

[a] All the clouds are included. Only the primary component is included for clouds with multiple components.

[b] Only clouds that are fit with one Gaussian are included.

[c] Only clouds that are fit with one Gaussian and have aspect ratio (the larger of ΔR.A./ΔDecl. and ΔDecl./ΔR.A.) less than 1.6 are included.

[d] The mean and median values are not derived due to small number of clouds in the smoothed Complex C data.

of the clouds have sizes of 10′–30′, corresponding to physical sizes of 30–100 pc. The median cloud size is 22′, corresponding to a physical size of 64.4 pc.

Figure 7 shows some of the physical properties of the clouds that depend on distance. The first two plots show the mass and size of the clouds versus line width. Clouds fit with double Gaussians are excluded from these plots. The relation between log(mass) and log(line width) is not very pronounced but the trend is that the larger the mass, the larger the line width. The slope of the linear fit is 0.08 ± 0.02 log(line width)/ log(mass). The relation between log(size) and log(line width) also shows a general trend that a larger size corresponds to a larger line width. The slope of the linear fit is 0.14 ± 0.03 log(linewidth)/ log(size). Given the selection effect of small and/or low-mass clouds with large line widths being difficult to detect, measurement of this slope should not be considered a significant result.

The bottom left panel shows the distribution of H I masses at 10 kpc for the cataloged clouds. The mass range extends from $10^{1.1}$–$10^{4.8}$ $M_\odot$. (Because there is only one cloud in the last

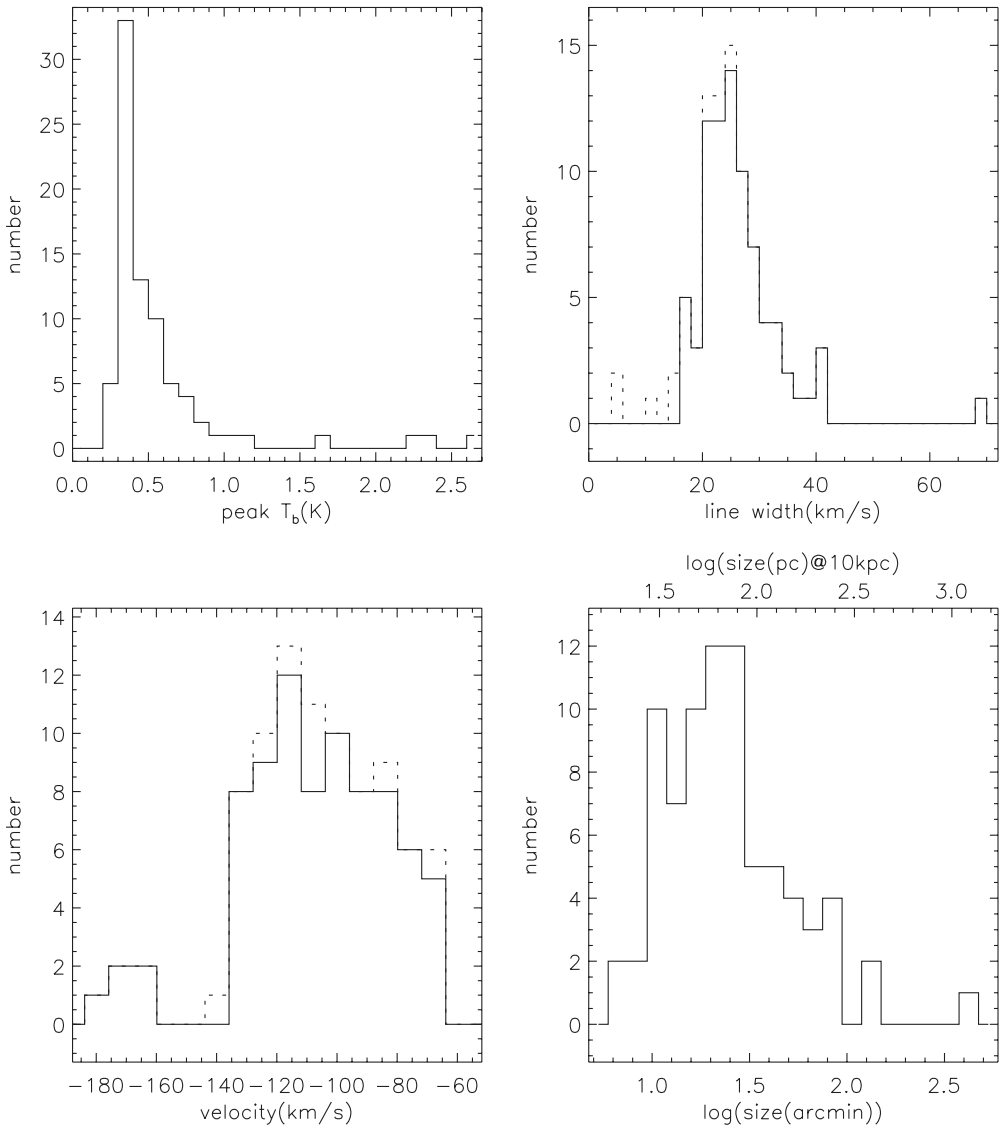


**Figure 6.** Statistics of the clouds in the Complex C cube (only the clouds with $V_{LSR} < -65$ km s$^{-1}$ are included). The plots are histograms of peak $T_b$ (K), line width, central velocity (LSR), and angular size and corresponding physical size at 10 kpc. The solid lines in the histograms represent the distribution of clouds that were fit with one Gaussian and the primary components of the clouds that were fit by two Gaussians (the component that contains more mass); the dashed lines include both components of the clouds fit with two Gaussians.

bin, it is not shown in this plot.) The mass distribution (given they are all placed at the same distance) follows a power law of slope of $-0.60 \pm 0.05$ $\log(N(\log(\text{mass})))/\log(\text{mass})$. The cutoff on the low end is determined by the noise level and the cutoff at the high end may be partially due to the limited spatial size of the cube. The drop in the number of clouds below $10^{1.6}$ $M_\odot$ is most likely due to catalog completeness and sensitivity limitations. In the case where the clouds were fit with two Gaussians, the sum of the two Gaussian components is used for the mass. The total H I mass of the clouds is $10^{5.0}$ $M_\odot$. The mass of the cataloged clouds is about 2% of the total mass of Complex C (approximately $M_{\rm H\,I} = 5 \times 10^6$ $M_\odot$; Thom et al. 2008).

The volume density distribution of the clouds is shown in Figure 12 (upper left). Since we do not have information on the size of the cloud in the third dimension, the clouds are assumed to be spherically symmetric, and the geometric mean of the size in R.A. and decl. is used for the diameter. Clouds that have an aspect ratio of greater than 1.6 are excluded from the density plots because they clearly violate the spherical symmetry assumption. The volume density ranges from 0.002 to 0.35 cm$^{-3}$, but the distribution has a prominent peak around 0.06 cm$^{-3}$, with a median volume density of 0.0645 cm$^{-3}$. About 60% of the clouds have a density between 0.01 and 0.08 cm$^{-3}$. The distribution of derived cloud pressures is shown in the lower left plot of Figure 12 (bottom axes), with most (59%) of the values being $P/k = 10^{2.6}$–$10^{3.1}$ K cm$^{-3}$ and the median value being $10^{2.8}$ K cm$^{-3}$.

#### *4.1.2. Smoothed Complex C clouds*

The search on the smoothed Complex C cube yields significantly fewer clouds as some small clouds are merged into larger clouds and some fall below the $5\sigma$ threshold after smoothing. Only 16 clouds are cataloged, and 2 of them required double Gaussian fitting to their total spectrum. Only clouds with

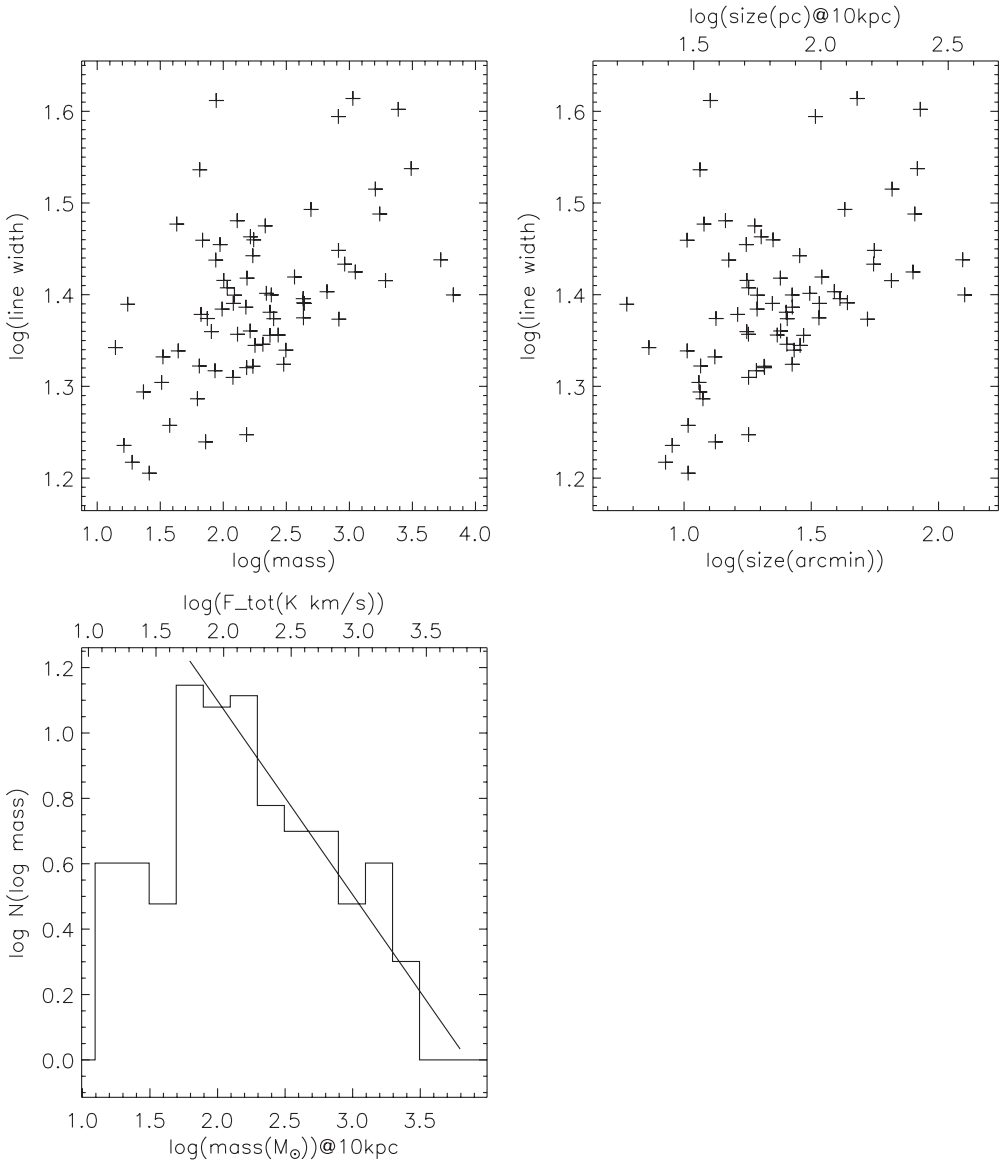


**Figure 7.** Statistics of the clouds in the Complex C cube (only the clouds with $V_{\rm LSR} < -65$ km s$^{-1}$ are included). The upper left plot shows line width vs. mass, and the upper right plot is line width vs. size. The clouds with two Gaussian components are removed from the plots for the line width vs. mass and the line width vs. size plots since no single line width can be defined. The lower left is a mass histogram at 10 kpc (slope $= -0.60 \pm 0.05$ log($N$(log(mass)))/ log(mass)).

$V_{\rm LSR} < -65$ km s$^{-1}$ are cataloged and included in the statistics.

Figure 8 shows the peak $T_b$, central velocity, line width, angular size, and corresponding physical size at 10 kpc for all of the cataloged clouds from the smoothed cube. The shape of the peak $T_b$ distribution is similar to that of the original cube, but the values are significantly smaller. This makes sense because when the cube is smoothed, the $T_b$ of the peak pixel is distributed to other pixels. The line width histogram has a peak at a similar velocity range as the full resolution catalog (24–28 km s$^{-1}$), with most clouds (67%) within 19–30 km s$^{-1}$ and a median value of 26.2 km s$^{-1}$. The velocity distribution of the clouds in the smoothed Complex C cube extends from $-130$ to $-80$ km s$^{-1}$. The few clouds at the highest velocities ($\sim -170$ km s$^{-1}$) in the original cube are merged into clouds of much higher flux at lower velocities and thus become a faint tail of high-velocity emission for a much larger cloud. Most of the clouds are between $-120$ and $-100$ km s$^{-1}$. The size distribution of the clouds is significantly larger, with the peak dictated by the spatial smoothing of the cube as expected. The median cloud size in the smoothed Complex C cube is 51.′7, corresponding to 150 pc at the distance of 10 kpc.

Figure 9 shows the mass and size of the clouds versus line width and the H I mass at 10 kpc. The relation between log(mass) and log(line width) is statistically indistinguishable from that of the original cube, though it is obviously greatly affected by low number statistics. The log(size) versus log(line width) plot is also statistically indistinguishable from that of the original cube. Since the smaller clouds are merged into larger clouds, the total H I masses are in general larger. The mass range of the clouds is $10^{1.9}$–$10^{4.9}$ $M_\odot$. Again the most massive cloud is not shown on this plot and for clouds fit with two Gaussians, the sum of the two Gaussians was used for the integrated intensity and mass. With the small number of clouds, it is not possible to determine if this distribution follows a power law. The total H I mass of the clouds is the same, $10^{5.0}$ $M_\odot$. The volume density of clouds in the smoothed cube is shifted to smaller values, though a very limited number of clouds satisfy our aspect ratio criteria

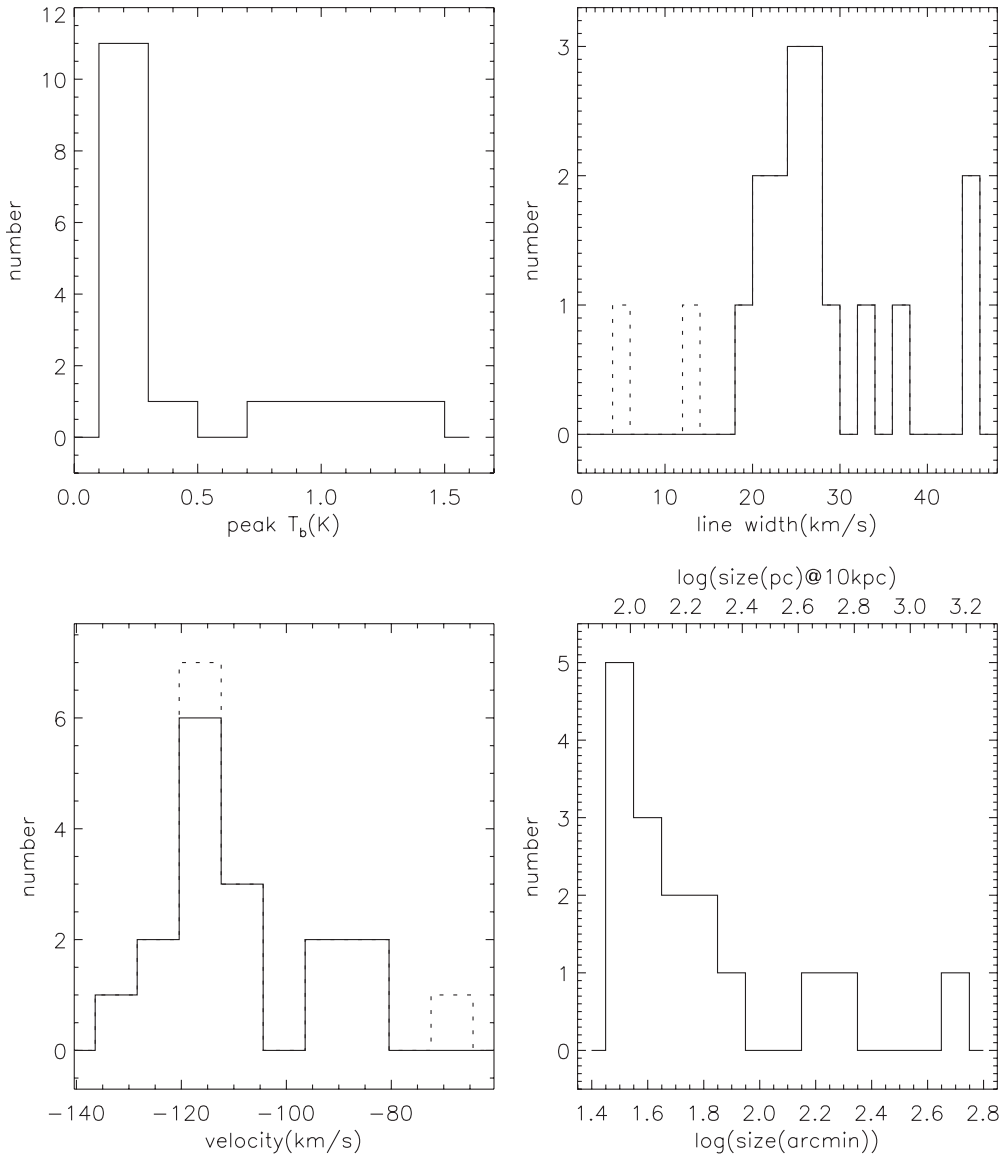


**Figure 8.** Statistics of clouds cataloged in the smoothed Complex C cube. The plots show histograms of peak $T_b$ (K), line width, central velocity (LSR), and size. The solid lines in the histograms represent the distribution of clouds that were fit with one Gaussian and the primary components of the clouds that were fit by two Gaussians (the component that contains more mass); the dashed lines include both components of the clouds fit with two Gaussians.

(13). This is expected as many clouds are merged together in the smoothing.

### 4.2. Magellanic Stream

Sixty-eight clouds were cataloged in the searched cubes containing the Magellanic Stream. Thirty-four clouds were found in region 1 and 38 were found in region 2 (see Section 2.1 or Figure 7 for the regions), with only 4 of the clouds requiring double Gaussian fitting. S08 also catalog clouds in these regions, but does so by eye. They find only 9 clouds in region 1 and 55 clouds in region 2. The discrepancies are due to two reasons: Duchamp is able to find smaller and fainter clouds that might be omitted in by-eye searches, and it counts two clouds as one if they are connected by diffuse emission that is above the grow threshold.

Figure 10 shows the peak $T_b$, central velocity, line width and size for all of the clouds cataloged. More than 90% of the clouds have a peak $T_b$ less than 0.6 K. The detection limit is 0.27 K for region 1, and 0.15 K for region 2. There is no evidence of a turnover in the distribution. The line width histogram spans from 10 to 65 km s$^{-1}$, but 75% of the clouds are found between 20 and 35 km s$^{-1}$, with a median line width of 27.7 km s$^{-1}$. The velocity distribution of the clouds in the Stream cube extends from −420 to −300 km s$^{-1}$ (LSR), with a peak at −350 km s$^{-1}$. In the GSR frame this range corresponds to −247 to −115 km s$^{-1}$. The sizes are shown in both arc minutes and the corresponding physical size at 60 kpc. The sizes of the clouds range from 6′ to 170′. Seventy percent of the clouds have sizes of 10′–30′, which corresponds to 170–510 pc at the assumed distance of 60 kpc. The median cloud size is 22.′1, corresponding to 376 pc (d/60 kpc).

The two upper plots of Figure 11 show the mass and size of the clouds versus line width. The relation between log(mass) and log(line width) is not very pronounced but the trend is that the larger the mass, the larger the line width. The slope of the linear fit is 0.12 ± 0.02 log(linewidth)/ log(mass). The relation

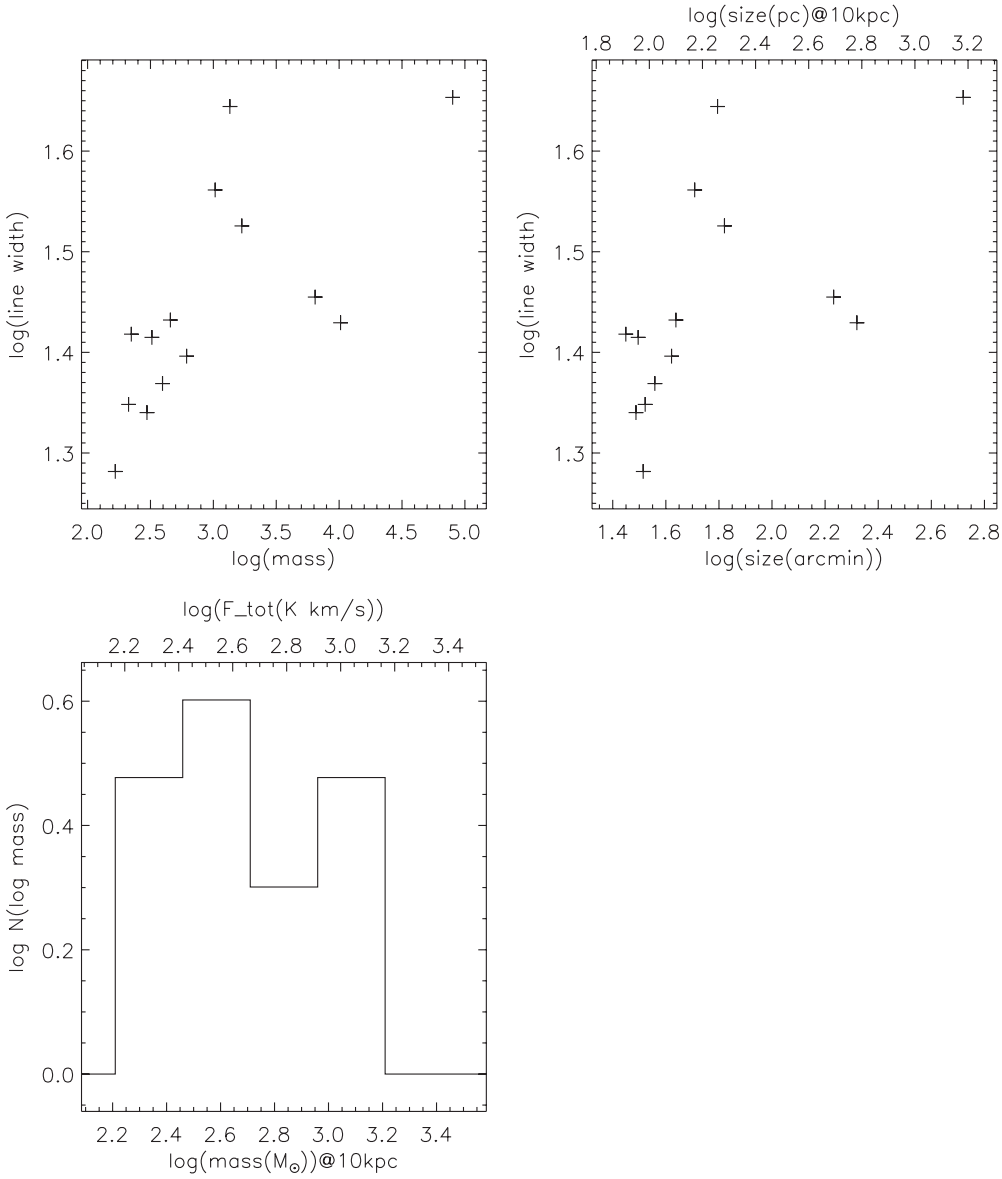


**Figure 9.** Statistics of smoothed Complex C clouds with $V_{LSR} < -65$ km s$^{-1}$ following the same format as Figure 8. The upper left and right plots show line width vs. mass and size, respectively. The bottom figure shows the distribution of masses at 10 kpc.

between log(size) and log(line width) also shows a general trend that the larger the size is, the larger the line width is. The slope of the linear fit is $0.23 \pm 0.04$ log(line width)/ log(size). As noted previously, selection effects are not taken into account for these slopes. The lower left corner of Figure 11 shows the distribution of H I masses at 60 kpc for all the cataloged clouds. The clouds extend over a mass range of $10^{2.4}$–$10^{5.5}$ $M_{\odot}$, and follow a power law of slope $-0.70 \pm 0.03$ log($N$(log(mass)))/ log(mass). The total H I mass of the clouds is $10^{6.1}$ $M_{\odot}$ (d/60 kpc)$^2$.

The upper right corner of Figure 12 shows the volume density distribution of the clouds if they are located at 60 kpc. The density ranges from 0.001 to 0.03 cm$^{-3}$, and 63% of the clouds have a density between 0.003 and 0.012 cm$^{-3}$. The median volume density is 0.009 cm$^{-3}$ (d/60 kpc)$^{-1}$. The distribution of derived cloud pressures is shown in the lower right plot of Figure 12 (bottom axis), with most (68%) of the values being $P/k = 10^{1.75}$–$10^{2.2}$ Kcm$^{-3}$ and the median value begin $P/k = 10^{1.9}$ K cm$^{-3}$(d/60 kpc)$^{-1}$.

## 5. DERIVATION OF PHYSICAL PROPERTIES: TESTS WITH SIMULATIONS

In this section we use a set of HVC simulations (see Heitsch & Putman 2009) to assess our choice of temperature (Section 5.1) and our derivations of cloud volume densities (Section 5.2) and pressures (Section 5.3). We examine the variation in these properties for a range of cloud models and viewing angles, i.e., the angle between cloud trajectory and the line of sight.

The details of the three-dimensional HVC simulations are published in Heitsch & Putman (2009), and the reader is referred to this paper for the details. The names of the HVC models in Figures 13–16 represent the various conditions tested for HVCs and the type of simulation. The beginning letter of W represents a simulation where the cloud is subjected to a wind of constant density to simulate the movement of the cloud through a diffuse, hot ($10^6$ K) halo medium, and the beginning letter of H represents a possibly more realistic setup, in which the cloud

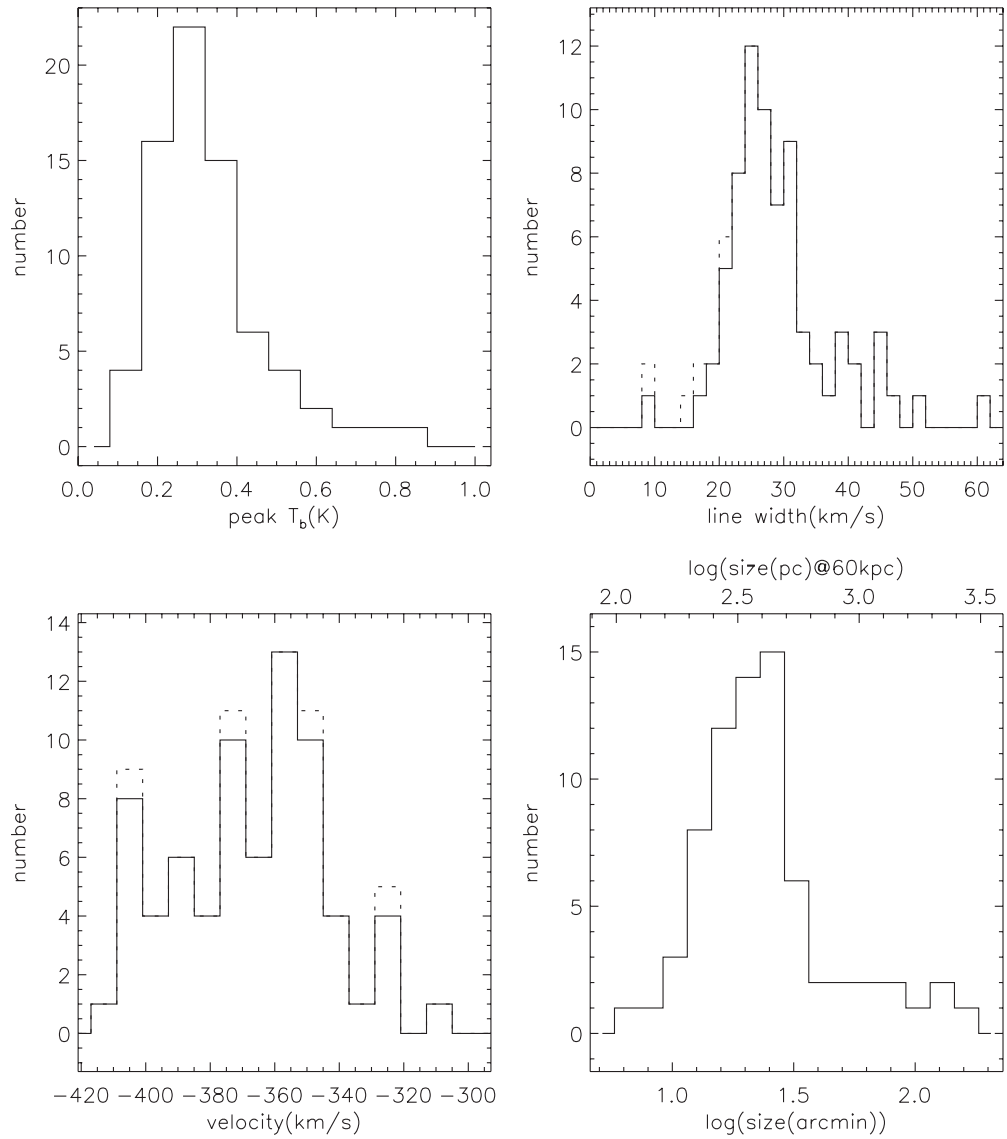


**Figure 10.** Statistics of Magellanic Stream clouds. The plots show histograms of peak $T_b$ (K), line width, central velocity (LSR), and size in both arc minutes and physical size at 60 kpc. The solid lines in the histograms represent the distribution of clouds that were fit with one Gaussian and the primary components of the clouds that were fit by two Gaussians (the component that contains more mass); the dashed lines include both components of the clouds fit with two Gaussians.

moves through a range of halo densities. The simulated cloud was setup to have typical observed cloud properties at a distance of 10 kpc, though we tested a range of halo densities as seen in Figure 16. For all simulations, the clouds are gradually disrupted by dynamical instabilities and we examine the clouds when they have developed a mild head–tail structure (i.e., somewhat elongated, but not beyond our aspect ratio of 1.6 limit when examined at high viewing angle values). The simulation data considered includes all HVC gas with $T < 10^4$ K, as a proxy for neutral hydrogen.

### 5.1. Thermal Line Width Assessment

The narrow distribution of line widths for HVCs is consistent with a warm neutral hydrogen component with a temperature of approximately 9000 K. We begin by assessing how the line widths may be affected by projection effects and any non-thermal component by "observing" several simulated clouds at viewing angles between 0 and 90 deg between the line of sight and the cloud trajectory. The "observed" line width for the simulated clouds can be represented by

$$\Delta_{\rm obs} = \sqrt{\Delta_{\rm nt}^2 + \Delta_{\rm th}^2}, \quad (1)$$

consisting of a non-thermal and thermal component.

Figure 13 demonstrates the effect of a variation in viewing angle on $\Delta_{\rm obs}$ compared to the thermal line width, $\Delta_{\rm th}$. The size of the symbols denotes the angle between the cloud trajectory and the line of sight for 90 (largest symbol), 60, 30, and 0 deg. In other words, the smallest symbols stand for clouds moving directly along the line of sight. The effect of an increase in viewing angle is the same in all models. The non-thermal component, or largely the disruption of the cloud in the form of a decelerated tail, increases as the viewing angle decreases. At large viewing angles, the line width is a close approximation of the thermal line width, while at small viewing angles the observed line width can differ by more than a factor of two in the extreme cases where the tail is a large fraction of the cloud's total mass. This comparison shows that the thermal line width is within a factor of 1.5 of the observed line width for over

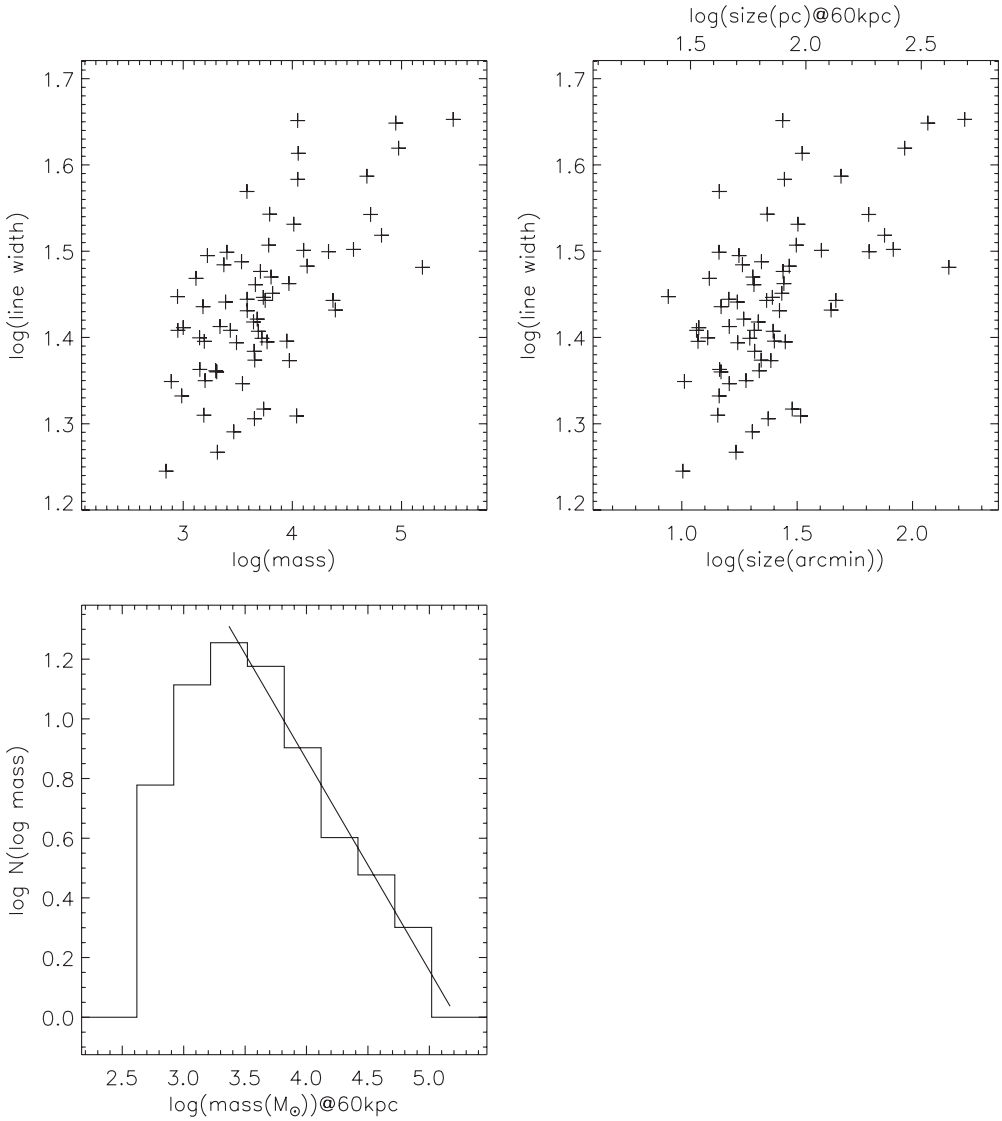


**Figure 11.** Statistics of Magellanic Stream clouds. The top two plots show line width vs. mass and size. The lower left plot shows mass at 60 kpc (slope $= -0.71 \pm 0.04$ $\log(N(\log(\text{mass})))/\log(\text{mass})$).

75% of the clouds. Going back to our observations, with our adopted cloud temperature of 9000 K, we expect a line width of $\sim$20 km s$^{-1}$ if it is entirely thermal. Since the vast majority of the GALFA-H I clouds have line widths between 20 and 30 km s$^{-1}$, the simulations indicate this temperature is consistent with the observed line width.

### 5.2. Dependence of Volume Density on Viewing Angle

Our derived volume densities can also be assessed by examining the simulation data at various viewing angles. Since as discussed we have set the temperature at 9000 K, the derived volume density is the only thing that causes a variation in our derived cloud pressure. The mean "true" volume density for each simulated cloud ($n_c$) is easily determined by averaging over the volume density of all gas with $T < 10^4$ K as a proxy for neutral hydrogen. To determine the "observed" volume density ($n_l$), we project each cloud for the angles 0, 30, 60, and 90 deg (as above), and determine the cloud mass by summing up the column densities of each resolution element. This mass $M_c$ is then used to determine the volume density, via

$$n_l = \frac{3M_c}{4\pi R^3}, \tag{2}$$

where we use

$$R = \sqrt{A/\pi}. \tag{3}$$

The cloud area $A$ is determined from the projection and we assume that our cloud is roughly spherical as in the derivation for the GALFA-H I clouds. As discussed above, the accuracy of the resulting density $n_l$ will thus depend on the elongation (or aspect ratio) of the cloud. Figure 14 shows the resulting $n_l$ against the actual mean cloud density $n_c$ as determined directly from the three-dimensional density field. Red symbols denote aspect ratios <1.6, i.e., the same selection criterion as used for the observed clouds. Most $n_l$ with this selection reproduce the "true" mean density within a factor of three.

### 5.3. Assessing Cloud Pressures

We use the adopted temperature and volume density to derive cloud pressures, so in this section we use the simulations

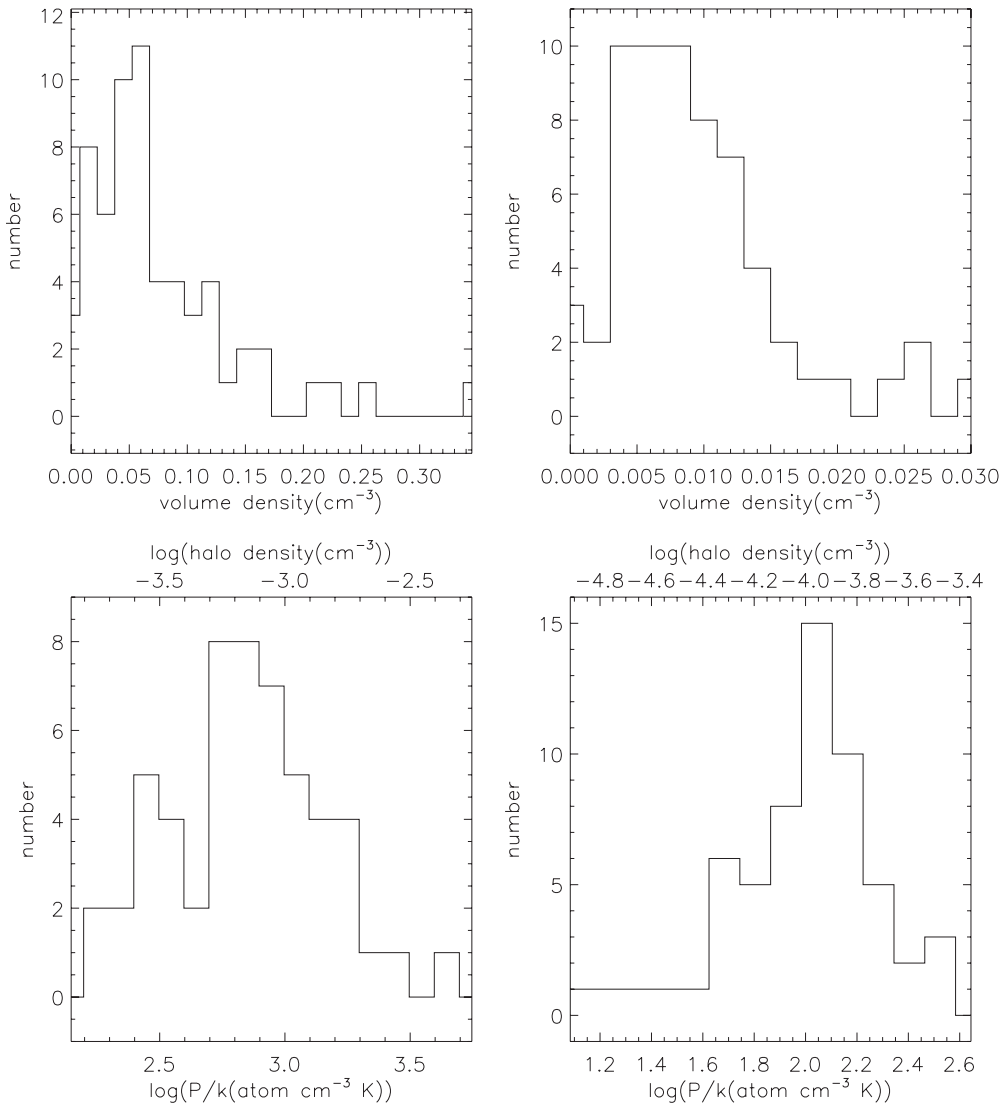


**Figure 12.** Top: volume density of the clouds in Complex C (left) and the MS (right) at 10 and 60 kpc, respectively. Bottom: derived pressure ($P/k$) and corresponding halo density required to confine the Complex C clouds (left) and MS clouds (right). The temperature of the Galactic halo is assumed to be $10^6$ K.

to compare the actual cloud pressures to deriving the cloud pressures in the same way we do for the GALFA-H I clouds. As noted in the previous two sections, viewing angle and variation in the cloud temperature are the two main factors that could lead to these values being different.

Figure 15 compares the actual thermal pressure within the three-dimensional simulated cloud to two other pressure estimates. The top panel shows actual thermal pressure, $P_{\rm th}$, against the derived pressure using the temperature of $T = 9000$ K and the "observed" volume density ($n_l$ from above), or

$$P_9 = k_B\, 9000\, n_l. \quad (4)$$

This plot shows that *underestimates* of the actual pressure (anything below the solid line) are due to large aspect ratios and subsequently too low of volume density (see Figure 14). Since we do not consider these clouds with large aspect ratios, this suggests we are unlikely to underestimate the pressure for the GALFA-H I clouds. The red symbols denoting aspect ratios $<1.6$ are in most cases *above* the solid line, indicating overestimates. Since almost all of the $n_l$ values are underestimates, *overestimates* must be caused by the temperature of 9000 K being too high. This is not surprising, given the lower thermal line width shown in Figure 13 and the fact that the model clouds consistently show a two-phase medium that is not evident in this population of GALFA-H I clouds (see Section 6.3). Therefore the overestimates in $P_9$ compared to $P_{\rm th}$ may be partially due to the simulated clouds having a lower average temperature (typically 6600–6700 K) than the GALFA-H I clouds.

The bottom panel shows the above $P_9$ estimate of the thermal pressure combined with the non-thermal component derived from the non-thermal line width,

$$P_{9t} = P_9 + 3 n_l\, \Delta^2_{\rm nt}. \quad (5)$$

The estimates are consistently higher as expected with the added non-thermal component, largely caused by the disrupted tail of the simulated cloud. Given, the non-thermal component is due to this decelerated tail, it cannot really be interpreted as a "turbulent pressure" and $P_9$ is the more accurate representation of the actual cloud pressure. The bottom panel also shows the spread between the minimum and maximum angle of one model is now larger than for $P_9$, since the lag between head and tail gets more dominant in velocity space with smaller angles.

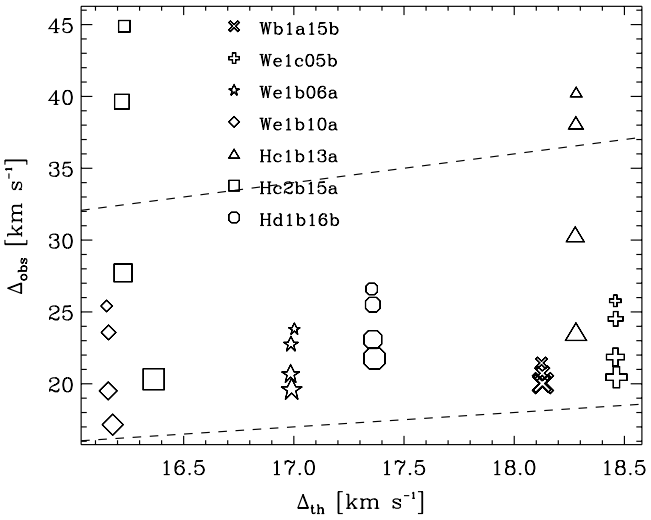


**Figure 13.** Total ("observed") line width ($\Delta_{obs}$) against thermal line width ($\Delta_{th}$) for a set of numerical model clouds (model names as used by Heitsch & Putman 2009). Symbol sizes denote the angle between cloud trajectory and line of sight, with the smallest symbol having the cloud coming at the observer (0 deg) and the largest symbol having the cloud traveling perpendicularly to the line of sight (90 deg). The dashed lines denote Mach numbers of 1 and 2.

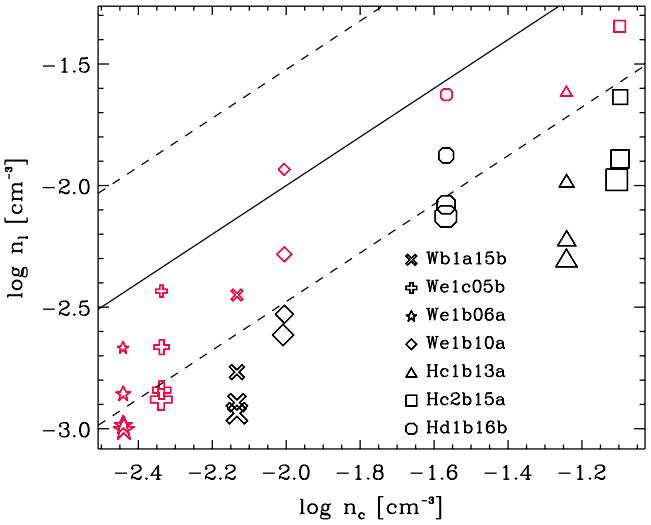


**Figure 14.** "Observed" volume density ($n_l$) derived from model cloud column density maps against "true" volume density ($n_c$) taken directly from the three-dimensional model clouds. Symbol sizes are as in Figure 13 and red symbols denote cloud aspect ratios <1.6. The solid line stands for $n_l = n_c$, with the dashed lines showing $3n_c$ and $n_c/3$.

(A color version of this figure is available in the online journal.)

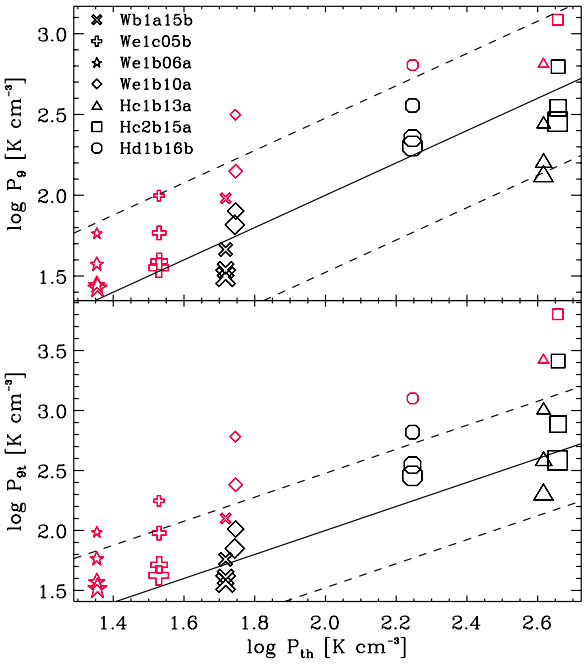


**Figure 15.** Two derivations of simulated cloud pressures, $P_9$ and $P_{9t}$ (see the text for a description), against the actual thermal pressure of the cloud, $P_{th}$. Red symbols indicate clouds with an aspect ratio <1.6 and symbol sizes are as in Figure 13. The solid line is the two pressures being equal and the dashed lines show $3P_c$ and $P_c/3$.

(A color version of this figure is available in the online journal.)

## 6. DISCUSSION

### *6.1. Comparison of the Complex C and Magellanic Stream Cloud Populations*

Since we know that the Magellanic Stream (MS) is gas stripped from the Magellanic Clouds (Mathewson et al. 1974), by comparing the properties of the Complex C and Magellanic Stream clouds we may gain insight into the origin of Complex C. Similar properties, such as density, mass, size, and line width distributions, may indicate a common physical process played a role in their origin. We compare the Stream clouds to both the original resolution Complex C cloud catalog and the smoothed Complex C cloud catalog. The smoothed catalog may be a better match to the clouds being resolved at the distance of the Magellanic Stream.

The line width distributions (Figures 6, 8, and 10) are similar for the MS and Complex C, except for a few outliers that may originate from the blending of two clouds along the line of sight. The typical line width of ∼20–30 km s$^{-1}$ is also found in other lower resolution HVC surveys (de Heij et al. 2002; Kalberla & Haud 2006), and therefore may indicate a common temperature for not only the MS and Complex C, but the majority of the HVCs. This line width is consistent with a temperature of ∼9000 K when the contribution of non-thermal broadening is considered (see Section 5.1). This is also discussed at length in terms of the thermal equilibrium gas temperature for HVCs in W95 and Wolfire et al. (1995a and 2003).

The Complex C data (Figure 6) and the MS data (Figure 10) have similar angular size distributions in the sense that both complexes show more small clouds than large clouds, with the smallest size limited by angular resolution. Since the physical size of the clouds scales with the distance, the cataloged MS clouds are shifted to larger physical sizes than that of Complex C (100–2900 (d/60 kpc) pc versus 17–1200 pc). For the smoothed Complex C cube the size distribution is shifted to 80–1500 pc, with the upper value limited by the area mapped.

In all the line width versus mass and line width versus size plots (shown in the top panels of Figures 7, 9 and 11) the scatter (∼0.1) is large compared to the overall range of the line width (∼0.4). Therefore the line width does not show clear correlations with the mass and the size of the clouds, and the slight trends (slope = 0.08 and 0.14, respectively, for Complex C and 0.12 and 0.23 for MS) are most likely due to selection effects. In contrast, molecular clouds generally show clear correlations of line width versus mass and line width versus size. Larson (1981) found a slope of 0.2 in line width versus mass and a slope of

0.38 in line width versus size. Recent observations give slopes of 0.4–0.5 in line width versus size (Elmegreen & Scalo 2004; Heyer & Brunt 2007). The difference is not surprising given the thermal line width is a significant component of the total line width of HVCs and the relations in molecular clouds are linked through assuming virialization which is unlikely to apply to HVCs (see Section 6.4).

The H I mass distribution is very similar for the original Complex C clouds and the MS clouds; they both show a power law distribution with a slope of −0.60 and −0.71, respectively. Though the MS cloud distribution is slightly steeper, the slopes are compatible within the statistical uncertainty. The total intensity range of the clouds in both catalogs is also very similar, although since the complexes are at different distances and the data have different sensitivities the range of masses is different. If the tail of the MS is at 60 kpc, the mass range probed in the MS is about 20 times higher than the mass range probed in Complex C at 10 kpc ($10^{2.4}$–$10^{5.5}$ versus $10^{1.1}$–$10^{4.8}$ $M_\odot$).

The median volume density of the MS clouds is seven times smaller than that of the Complex C clouds (top panels of Figure 12, again assuming that Complex C is at 10 kpc and the MS is at 60 kpc). Since both the Complex C and MS clouds have a similar range of line widths, the difference in their densities may be reflected in the cloud pressures. The median pressure ($P/k$) derived for Complex C clouds is $\sim 10^{2.8}$ K cm$^{-3}$, which is about six times greater than that of the median MS cloud at $\sim 10^{1.9}$ K cm$^{-3}$ (see bottom panels of Figure 12). The pressures derived are consistent with the work of Wolfire et al. (1995a). The calculations of volume density and pressure are assessed in Section 5 through comparison with simulations and it is found that the effect of the viewing angle and the pressure assumptions can cause these values to vary by up to a factor of three. This is expected to dominate over other uncertainties given the 13 clouds in the smoothed Complex C cube (showing the effect of a bigger beam and higher sensitivity) results in volume densities less than a factor of three lower. Given our large sample of clouds for original Complex C cube and the MS, we do not expect the entire population to be affected by viewing angle or beam dilution and the distributions will remain distinct.

We note here that the distance to the tail of the Magellanic Stream remains uncertain and this will scale the MS values accordingly. For simplicity, we have put the tail at roughly the distance of the Magellanic Clouds, though many models have the tail at larger distances. The tidal stripping models often put the tail of the Stream at distances of approximately 100–200 kpc (e.g., Connors et al. 2006) and models based on recent proper motion calculations indicate the Magellanic Clouds may be on their first passage and that the tail of the Stream is at ∼120 kpc (Besla et al. 2007). If the Stream is as distant as 120 kpc the most massive clouds cataloged here would be at $M_{\rm H\,I} = 10^{6.1}$ $M_\odot$, or half as massive as the entire Complex C and 1′ would correspond to a physical size of 35 pc. The median volume density and pressure would shift to 0.005 cm$^{-3}$ and 42 (K cm$^{-3}$) at 120 kpc.

Though the absolute values for the sizes and masses of the Magellanic Stream clouds depend on the actual distance ($d$ for the size and $d^2$ for the mass), the slopes of the distributions will not change, and therefore will remain similar to the slopes of the Complex C cloud distributions. This includes the original and smoothed Complex C cloud distributions, although there are a limited number of clouds in the smoothed cube. The relatively narrow distribution of line widths found here suggests the clouds have a common warm temperature component, and their size may be dictated by the surrounding pressure and cloud mass. Overall, the similarities in the MS and Complex C distributions are intriguing and may suggest a similar formation or destruction mechanism for the two complexes, despite their different locations in the Galaxy's halo. The results also suggest that smaller and lower mass clouds will be detected for both complexes as deeper and higher resolution surveys are completed.

### 6.2. Comparison of Complex C Clouds to Galactic Disk–Halo Clouds

In the Complex C cube, clouds can be cataloged from high negative velocities (∼ − 180 km s$^{-1}$) into Galactic emission where it becomes difficult to distinguish individual clouds. This may represent the accretion and breaking up of Complex C as it is approaching the disk, or simply an overlap between the population of clouds in Complex C and at the disk–halo interface. In any case, a comparison between the properties of the clouds associated with HVCs and those that are at the disk–halo interface is an interesting exercise, as it may provide insight into whether the clouds represent similar gas at different stages of the accretion process.

There are several studies of clouds at the disk–halo interface in the literature. The study of the disk–halo clouds on the positive velocity side of the GALFA-H I Complex C cube will appear in another paper, but a population of discrete disk–halo clouds in this general region was found and discussed by Lockman (2002). He found that these clouds follow Galactic rotation and are discrete in position and velocity, with typical sizes of a few tens of parsecs. Stil et al. (2006) and Ford et al. (2008) derived the statistical properties of additional clouds that are most likely at the disk–halo interface using the Very Large Array Galactic Plane Survey and the Parkes Galactic All-Sky Survey. The tangent point method was used to derive the distance to the clouds, and properties such as mass and physical size were subsequently derived. The typical size and mass are similar to a smaller Complex C cloud, with the mass distribution peaking around a median mass of 600–700 $M_\odot$. The mass distribution does not show the power-law distribution we see for both Complex C and the Magellanic Stream, but this may be due to the selection of the disk–halo clouds as discrete and unrelated spatially, while we are studying all clouds related to a single complex. Stanimirović et al. (2006) observed disk–halo clouds in the outer Galaxy toward the Galactic anticenter with GALFA-H I. Since these observations are taken with the same instrument as the data used in this work, the angular and velocity resolution are the same, allowing a direct comparison of the cloud properties. These clouds are in general colder than the Complex C and MS clouds, with an average kinetic temperature of ∼470 K. On average, disk–halo clouds have smaller line widths ($\Delta V \approx 13$km s$^{-1}$ for a median cloud in Ford et al. 2008; $\Delta V \approx 4$km s$^{-1}$ for a median cloud in Stanimirović et al. 2006) compared to the typical HVC value of 25 km s$^{-1}$, suggesting a lower temperature. A more complete census of disk–halo clouds is being completed with the GALFA-H I Survey, and this will allow for more thorough comparisons of the cloud populations.

### 6.3. Clouds with Multi-phase Structure

Multiple components in the line profiles of HVCs are commonly observed (e.g., Kalberla & Haud 2006) and have been explained as the existence of a two-phase structure from calculations of the thermal equilibrium temperature for neutral hydrogen gas under different conditions (W95). W95 considered

the conditions under which thermally bi-stable structures can exist and discussed the corresponding physical environments. In our Complex C catalog, only eight clouds (10%) require a two component fit to the line profile. Following S08, we consider the clouds in our catalog to have a multi-phase structure only when the absolute difference between the $V_{\rm LSR}$ of the two components is smaller than the $\Delta V$ of the primary component. This excludes cataloged clouds with two components due to multiple clouds along the line of sight. For Complex C all eight (10%) of the clouds with a two component fit satisfy this criterion. In the Magellanic Stream data, only four of the clouds (6%) require a two component fit, and all of them satisfy the criterion for multi-phase structure.

Since the number of clouds requiring a multiple Gaussian fit to the line profile is lower than that found in previous studies (e.g., S08), we also looked at the line profile at the peak pixel of the cloud. We were originally considering the integrated spectrum over the whole cloud, which might wash out the narrow-component of the cloud due to velocity structure across the cloud. With the line profile fit to the cloud's peak pixel, the percentage of clouds in the Stream catalog that require two-component fitting is similar to that found by S08 (15%). This serves as a reality check, showing that the fitting criteria are similar. In the case of the Complex C cloud, when only the peak pixel is considered the same number of clouds require two-component fitting, or 7% of the total. This is consistent with the findings of Kalberla & Haud (2006) using the Leiden/Argentina/Bonn (LAB) Survey with a factor of 10 larger beam than our survey. They found that about 7.5% of the observed positions have multi-component line profile structure in the negative velocity part of the MS, and only 6% of the positions in Complex C. It should be noted that we only consider the spectra at the peak pixel of each cloud and Kalberla & Haud (2006) considered the spectra of all observed positions.

W95 find in general that in a higher density halo medium a two component profile, or core-halo structure, is expected for the HVCs. It is therefore counterintuitive that the multi-phase structure is not more prominent in Complex C given that it is closer to the plane of the Galaxy. The slightly lower sensitivity of the Complex C cube compared to the Stream regions is unlikely to account for this difference, as we also fit the peak pixel of the smoothed Complex C cube, which has a higher sensitivity, and there are still few clouds with two-phase structure. In contrast to Complex C, at the $z$-height of the Magellanic Stream, a two-phase structure is not expected, as largely observed.

One possible explanation is the role of dust content and metallicity in determining the cooling curve (W95). Complex C has a metallicity range between 0.1 and 0.5 solar across the cloud (Gibson et al. 2001; Collins et al. 2003, 2007; Tripp et al. 2003), but seems to have little or no dust (Richter et al. 2001; Peek et al. 2009). For, reference, the gas associated with the Magellanic System has a metallicity of about 0.2–0.4 and appears to have some dust (Gibson et al. 2000; Sembach et al. 2001). To understand whether two-phase structure should exist in Complex C, we follow the analysis outlined by W95 and Wolfire et al. (2003, hereafter W03) and calculate the thermally stable condition at the tail of Complex C.

We adopt the standard photoelectric heating rate given by W03. The heating from the FUV field can be written as a combination of the radial FUV intensity given by Equation (14) in W03 and the vertical variation given by Equation (4) in W95, with the out-of-plane FUV intensity 0.6 times that of the midplane (W95). Since cosmic ray heating is consistently approximately an order of magnitude lower than FUV/X-ray heating it is not considered here. At low temperatures, the dominant cooling process in the cold phase is radiative line cooling of the [C II] 158 $\mu$m fine-structure transition, while at higher temperatures, cooling is the result of several lines: [C II] 158 $\mu$m, [O I] 163 $\mu$m, and Ly$\alpha$. The cooling rate for each of these species using a metallicity of 0.3 solar is given by W03. In this simple model of heating and cooling in Complex C, a multi-phase structure is predicted to exist. At $\log(P/k) = 3$, Complex C has two thermally stable equilibrium temperatures, a cold and warm component. Observationally, the majority of the clouds in this region of Complex C show only the warm component.

The fact that the Complex C clouds show only the warm component may be due to a combination of long cooling times and the dynamic, turbulent environment of the complex. The dominant coolant [C II] has a cooling rate on the order of $2 \times 10^{-28}$ erg s$^{-1}$ around n $\approx 0.06$ cm$^{-3}$, the median density we found for the Complex C clouds. The cooling time is then approximately tc $\approx$ [(3/2) kT]/($2 \times 10^{-28}$ erg s$^{-1}$) $\approx 300$ Myr. This is long compared to the typical lifetimes expected for halo clouds moving through a diffuse halo medium (generally <80 Myr; Heitsch & Putman 2009). Therefore the clouds may not live long enough to cool substantially and form a two-phase structure.

### 6.4. Inference on Halo Density

HVCs are often assumed to be in pressure equilibrium with the surrounding hot halo medium, and we use that assumption here to infer the density of the diffuse gaseous halo. The clouds are unlikely to be gravitationally confined, as using $M_{\rm dyn} \geqslant R\Delta V^2/8G$ and the typical properties of Complex C clouds ($R = 10^{1.7}$ pc, $\Delta V = 25$km s$^{-1}$), we find a mass 1000 times greater than $M_{\rm H\,I}$ ($\sim 10^{2.2}$ $M_\odot$). This is also consistent with the lack of line-width-mass correspondence (Figures 7, 9, and 11). Assuming pressure balance between the cloud and the confining halo medium, the external pressure is given by $P_h = kn_hT_h$, where $T_h$ is the halo temperature and is assumed to be $10^6$ K, and $n_h$ is the halo density. As outlined in Section 4, the thermal pressure of the cloud is given by $P_c = kn_cT_c$, where $T_c$ is the cloud temperature set at 9000 K, and $n_c$ is the cloud volume density for clouds with an aspect ratio less than 1.6.

Figure 12 shows the pressure of the clouds in units of $(P/k)$ and the halo density required to confine each cloud if they are in pressure equilibrium. The required halo densities lie within a reasonable range. For Complex C at a distance of 10 kpc or $\sim$8 kpc from the Galactic Center and a $z$-height of 2–4 kpc, $P/k$ is typically $10^{2.6}$–$10^{3.1}$ K cm$^{-3}$. This corresponds to a halo density range of $10^{-3.3}$–$10^{-3}$ cm$^{-3}$ at a temperature of $10^6$ K. The scatter in the inferred halo density most likely shows the uncertainty in the spherical symmetry and pressure equilibrium assumptions, rather than indicating a large variation in halo density.

We can do the same analysis for the Magellanic Stream, with the consideration that the distance is more uncertain for the tail of this complex. At the assumed distance of 60 kpc, or a $z$-height of $\sim$40 kpc, $P/k$ is typically $10^{1.75}$–$10^{2.2}$ K cm$^{-3}$, corresponding to a typical halo density of $10^{-4.1}$–$10^{-3.7}$ cm$^{-3}$. This value is consistent with the results of previous studies of the Magellanic Stream (Stanimirović et al. 2002). Note that if we change the distance by a factor of two, $P/k$ and halo density would change by a factor of two as well. Therefore if the tail

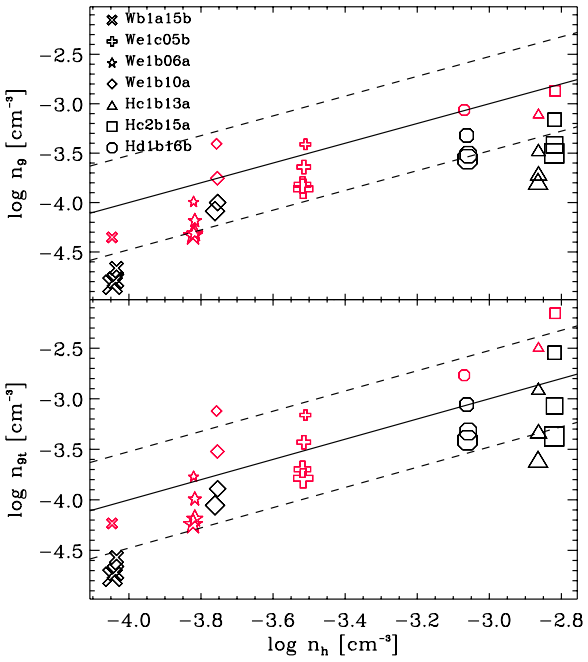


**Figure 16.** Derived halo densities from the cloud simulations, $n_9$ and $n_{9t}$ (see the text), compared to the actual halo density in the simulation, $n_h$. The derived halo densities are based on the pressure estimates in Figure 15. As in previous plots the red symbols indicate clouds with an aspect ratio <1.6, symbol sizes are as in Figure 13, the solid line is the two halo densities being equal and the dashed lines show $3n_h$ and $n_h/3$.

(A color version of this figure is available in the online journal.)

of the Stream is actually at 120 kpc, the surrounding confining halo density would need to be only $10^{-4.4}$–$10^{-4.0}$ cm$^{-3}$.

In Section 5 we assess the use of our derived volume density and temperature value to obtain a cloud pressure through an investigation of cloud simulations "observed" from various viewing angles. We can now compare the actual halo densities in the simulations to values obtained by setting the thermal pressure of the surrounding halo gas to the observed cloud pressures ($P_9$ and $P_{9t}$ from Section 5.3). The results of the comparisons are shown in Figure 16. The top panel shows the halo densities ($n_9$) derived using the $P_9$ cloud pressures (similar to the pressures derived for the GALFA-H I clouds) versus the actual halo density ($n_h$). The clouds with the smallest aspect ratios give the best estimates, though all of the clouds that fit into our aspect ratio cut are within a factor of three of the actual halo density. In the top panel the derived halo density is almost always lower than the actual halo density. The bottom panel shows the halo densities ($n_{9t}$) obtained using $P_{9t}$ values, or $P_9$ plus a possible pressure contribution from the non-thermal line width, against $n_h$. The clouds with the smallest aspect ratios shift to being overestimates of the halo density, consistent with the non-thermal line width not representing a form of pressure that should be included in the analysis. As with $P_{9t}$, the scatter also increases for $n_{9t}$ compared to $n_9$.

Our derived halo density estimates can be compared to values obtained from other observations and from simulations. Observationally, estimates of halo density have been derived from pulsar dispersion measures, O VI and O VII observations, and HVC structures. The pulsar dispersion measures are thought to be a direct way to detect the halo medium. Gaensler et al. (2008) derived the $3\sigma$ upper limit of the halo density to be $10^{-3.1}$ cm$^{-3}$ from pulsar dispersion measures at $z > 5$ kpc. They also derived the distribution of the warm ionized medium to be $n(z) = 0.031 \exp(-z/1\,\mathrm{kpc})$ cm$^{-3}$, which gives a density of $10^{-2.8}$ cm$^{-3}$ at $z \sim 3$ kpc. This is consistent with the halo density we derive. At the distance of the Stream, the halo density we derive is consistent with O VI and O VII observations (Bregman & Lloyd-Davies 2007; Sembach et al. 2003) and the densities needed to strip gas from dwarf galaxies (Grcevich & Putman 2009).

On the theoretical side, models of the distribution of hot diffuse halo gas are generally spherical. Both ΛCDM cosmological simulations and analytical approximations of a Milky Way-like galaxy predict a halo density of $\sim 10^{-3}$–$10^{-3.8}$ cm$^{-3}$ at 10 kpc (Maller & Bullock 2004; Sommer-Larsen 2006; Kaufmann et al. 2008). These values are roughly consistent with our halo density estimates from the Complex C observations at ~8 kpc from the Galactic center, though these simulations are not designed to accurately represent the region near the disk. At 50 kpc, the predicted density from the simulations is about $\sim 10^{-4.2}$–$10^{-3.5}$ cm$^{-3}$, which is similar to our estimate from the Magellanic Stream. It should be noted that if the halo temperature is actually closer to $2 \times 10^6$ our halo densities will decrease by a factor of two. This is likely to be a larger effect than a small variation in the temperature of the warm halo clouds.

## 7. CONCLUSIONS

This paper presents new H I observations of the tail of Complex C from the GALFA-H I Survey. The observations have 3.′5 spatial resolution and 0.18 km s$^{-1}$ channel spacing, smoothed to 1.4 km s$^{-1}$ for this work. We catalog discrete clouds at the tip of Complex C and the Magellanic Stream with Duchamp, an automated source finder that provides a systematic and objective way of cataloging clouds. Diffuse Galactic emission was removed from the Complex C data before cataloging to enable us to search for clouds at lower velocity and obtain accurate H I column densities for the clouds. The cloud spectra are fit with Gaussian profiles to obtain their LSR velocities, FWHM values, and column densities and, given we have a distance for Complex C and a distance estimate for the Magellanic Stream, their physical properties are derived, including mass, size in parsecs, volume density, and pressure. We then compare the physical properties of the clouds in the Magellanic Stream and Complex C (including the original cube and a smoothed cube to approximate Complex C at a distance more appropriate to the Magellanic Stream), and derive the density of the surrounding halo medium assuming pressure balance. Finally we test the derived properties with three-dimensional simulations of clouds moving through a diffuse medium. Several of the main results can be summarized as follows:

1. The Complex C and Magellanic Stream clouds show similarities in their line width, angular size, and mass distributions. The common line width of ~25km s$^{-1}$ is found for HVCs in general and is indicative of a warm component for the clouds. Both complexes show a power-law distribution of mass above the detection limit. The Complex C clouds have a mass distribution of slope $= -0.60 \pm 0.05$ and the Magellanic Stream clouds have a slope $= -0.71 \pm 0.04$. The clouds in the two complexes do not show any distinctive differences and the similarities suggest a similar origin of formation or common physical process breaking down the clouds. This is despite their different halo environments in terms of distance and the derived surrounding pressure.

2. The Complex C clouds have a median $T_{b,\mathrm{peak}}$ of 0.41 K, median line width of 24.9 km s$^{-1}$, median $V_{\mathrm{LSR}}$ of $-105$ km s$^{-1}$, and median size of 22.′2, corresponding to 64.4 pc at a distance of 10 kpc. The smoothed Complex C clouds have a median $T_{b,\mathrm{peak}}$ of 0.18 K, median line width of 26.2 km s$^{-1}$, median $V_{\mathrm{LSR}}$ of $-113$ km s$^{-1}$, and median size of 51.′7, corresponding to 150 pc at a distance of 10 kpc. The MS clouds have a median $T_{b,\mathrm{peak}}$ of 0.30 K, median line width of 27.7 km s$^{-1}$, median $V_{\mathrm{LSR}}$ of $-364$ km s$^{-1}$, and median size of 22.′1, corresponding to 376 (d/60 kpc) pc.
3. From Gaussian fitting of the line profiles, it is found that neither the Magellanic Stream or Complex C clouds have abundant two-phase structure (7% of the clouds). Following the analysis of W03 and W95 we confirm that a two-phase structure is expected in the environment of Complex C. The lack of this structure may be explained by the fact that Complex C has a low metallicity and thus the cooling time is long compared to a typical cloud's lifetime.
4. Assuming that the clouds are confined by the pressure of the surrounding hot halo medium, we estimate the density of the hot halo medium at the $z$-height of the tail of Complex C ($\sim$3 kpc) is $10^{-3.3}$–$10^{-3.0}$ cm$^{-3}$, with a median value of $5.8 \times 10^{-4} = 10^{-3.2}$ cm$^{-3}$. For the Magellanic Stream we obtain values of $10^{-4.1}$–$10^{-3.7}$ cm$^{-3}$ (with a median value of $10^{-4.1}$ cm$^{-3}$) at a $z$-height of 40 kpc, and this would scale down by a factor of two if the distance is a factor of two greater. These estimates are consistent with previous observations and models of the Galactic halo.
5. We assess the derived physical properties or our clouds with simulations. We justify the use of a constant temperature of 9000 K, as well as a selection of an aspect ratio of $<$1.6 for deriving the volume densities, pressures, and halo densities from the clouds. The analysis finds that these properties are accurate to within a factor of three.

We thank Jana Grcevich for help with the observations, Kevin Douglas for help with the data reduction, and the rest of the GALFA-H I Survey team for the development of the tools that helped in the collection and reduction of these data. This research made use of the Duchamp source finder, produced at the Australia Telescope National Facility, CSIRO, by M. Whiting. M.E.P., S.S., and J.E.G.P. acknowledge support from NSF grants AST-0707597/0917810, 0707679, and 0709347. F.H. acknowledges support from NSF grant AST-0807305. M.E.P. also acknowledges support from the Research Corporation. We credit the use of the Karma visualization software (Gooch 1996). The Arecibo Observatory is part of the National Astronomy and Ionosphere Center, which is operated by Cornell University under a cooperative agreement with the National Science Foundation.

## REFERENCES

Besla, G., Kallivayalil, N., Hernquist, L., Robertson, B., Cox, T. J., van der Marel, R. P., & Alcock, C. 2007, ApJ, 668, 949
Bregman, J. N. 1980, ApJ, 236, 577
Bregman, J. N., & Lloyd-Davies, E. J. 2007, ApJ, 669, 990
Brüns, C., Kerp, J., Kalberla, P. M. W., & Mebold, U. 2000, A&A, 357, 120
Chiappini, C., Matteucci, F., & Romano, D. 2001, ApJ, 554, 1044
Collins, J. A., Shull, J. M., & Giroux, M. L. 2003, ApJ, 585, 336
Collins, J. A., Shull, J. M., & Giroux, M. L. 2007, ApJ, 657, 271
Connors, T. W., Kawata, D., & Gibson, B. K. 2006, MNRAS, 371, 108
de Heij, V., Braun, R., & Burton, W. B. 2002, A&A, 391, 159
Elmegreen, B. G., & Scalo, J. 2004, ARA&A, 42, 211
Fenner, Y., & Gibson, B. K. 2003, PASA, 20, 189
Ford, H. A., McClure-Griffiths, N. M., Lockman, F. J., Bailin, J., Calabretta, M. R., Kalberla, P. M. W., Murphy, T., & Pisano, D. J. 2008, ApJ, 688, 290
Fraternali, F., & Binney, J. J. 2008, MNRAS, 386, 935
Gaensler, B. M., Madsen, G. J., Chatterjee, S., & Mao, S. A. 2008, PASA, 25, 184
Gibson, B. K., Giroux, M. L., Penton, S. V., Putman, M. E., Stocke, J. T., & Shull, J. M. 2000, AJ, 120, 1830
Gibson, B. K., Giroux, M. L., Penton, S. V., Stocke, J. T., Shull, J. M., & Tumlinson, J. 2001, AJ, 122, 3280
Gooch, R. 1996, in ASP Conf. Ser. 101, Astronomical Data Analysis Software and Systems V, ed. G. H. Jacoby & J. Barnes (San Francisco, CA: ASP), 80
Grcevich, J., & Putman, M. E. 2009, ApJ, 696, 385
Heiles, C. 2007, PASP, 119, 643
Heitsch, F., & Putman, M. E. 2009, ApJ, 698, 1485
Heyer, M. H., & Brunt, C. 2007, in IAU Symp., Vol. 237, ed. B. G. Elmegreen & J. Palous, 9
Kalberla, P. M. W., & Haud, U. 2006, A&A, 455, 481
Kaufmann, T., Bullock, J. S., Maller, A., & Fang, T. 2008, in ASP Conf. Ser. 396, Formation and Evolution of Galaxy Disks, ed. S. J. José, G. Funes, & E. M. Corsini (San Francisco, CA: ASP), 439
Kaufmann, T., Mayer, L., Wadsley, J., Stadel, J., & Moore, B. 2006, MNRAS, 370, 1612
Kereš, D., & Hernquist, L. 2009, ApJ, 700, L1
Larson, R. B. 1981, MNRAS, 194, 809
Lockman, F. J. 2002, ApJ, 580, L47
Maller, A. H., & Bullock, J. S. 2004, MNRAS, 355, 694
Mathewson, D. S., Cleary, M. N., & Murray, J. D. 1974, ApJ, 190, 291
Peek, J. E. G., & Heiles, C. 2008, arXiv:0810.1283P
Peek, J. E. G., Heiles, C., Putman, M. E., & Douglas, K. 2009, ApJ, 692, 827
Peek, J. E. G., Putman, M. E., McKee, C. F., Heiles, C., & Stanimirović, S. 2007, ApJ, 656, 907
Peek, J. E. G., Putman, M. E., & Sommer-Larsen, J. 2008, ApJ, 674, 227
Putman, M. E., Staveley-Smith, L., Freeman, K. C., Gibson, B. K., & Barnes, D. G. 2003, ApJ, 586, 170
Putman, M. E., et al. 2009, ApJ, 703, 1486
Richter, P., Sembach, K. R., Wakker, B. P., Savage, B. D., Tripp, T. M., Murphy, E. M., Kalberla, P. M. W., & Jenkins, E. B. 2001, ApJ, 559, 318
Robitaille, T. P., & Whitney, B. A. 2010, ApJ, 710, L11
Sembach, K. R., Howk, J. C., Savage, B. D., & Shull, J. M. 2001, AJ, 121, 992
Sembach, K. R., et al. 2003, ApJS, 146, 165
Shapiro, P. R., & Field, G. B. 1976, ApJ, 205, 762
Sommer-Larsen, J. 2006, ApJ, 644, L1
Stanimirović, S., Dickey, J. M., Krčo, M., & Brooks, A. M. 2002, ApJ, 576, 773
Stanimirović, S., Hoffman, S., Heiles, C., Douglas, K. A., Putman, M., & Peek, J. E. G. 2008, ApJ, 680, 276
Stanimirović, S., et al. 2006, ApJ, 653, 1210
Stil, J. M., et al. 2006, ApJ, 637, 366
Thom, C., Peek, J. E. G., Putman, M. E., Heiles, C., Peek, K. M. G., & Wilhelm, R. 2008, ApJ, 684, 364
Tripp, T. M., et al. 2003, AJ, 125, 3122
Wakker, B. P., et al. 1999, Nature, 402, 388
Wakker, B. P., et al. 2007, ApJ, 670, L113
Whiting, M. T. 2008, in Galaxies in the Local Volume, ed. B. S. Koribalski & H. Jerjen (Berlin: Springer), 343
Wolfire, M. G., Hollenbach, D., McKee, C. F., Tielens, A. G. G. M., & Bakes, E. L. O. 1995a, ApJ, 443, 152
Wolfire, M. G., McKee, C. F., Hollenbach, D., & Tielens, A. G. G. M. 1995b, ApJ, 453, 673
Wolfire, M. G., McKee, C. F., Hollenbach, D., & Tielens, A. G. G. M. 2003, ApJ, 587, 278